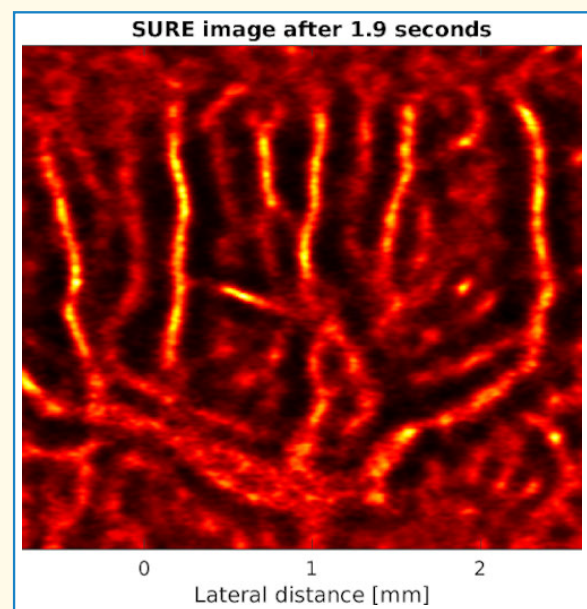


Super-Resolution Ultrasound Imaging Using the Erythrocytes—Part I: Density Images

Jørgen Arendt Jensen¹, *Fellow, IEEE*, Mostafa Amin Najji², *Graduate Student Member, IEEE*, Sebastian Kazmarek Præsius³, *Graduate Student Member, IEEE*, Iman Taghavi, *Member, IEEE*, Mikkel Schou⁴, *Member, IEEE*, Lauge Naur Hansen⁵, *Graduate Student Member, IEEE*, Sofie Bech Andersen, Stinne Byrholdt Søgaard⁶, Nathalie Sarup Panduro⁷, Charlotte Mehlin Sørensen⁸, Michael Bachmann Nielsen⁹, Carsten Gundlach, Hans Martin Kjer¹⁰, Anders Bjorholm Dahl, *Member, IEEE*, Borislav Gueorguiev Tomov¹¹, *Member, IEEE*, Martin Lind Ommen¹², *Member, IEEE*, Niels Bent Larsen¹³, *Member, IEEE*, and Erik Vilain Thomsen¹⁴, *Member, IEEE*

Abstract—A new approach for vascular super-resolution (SR) imaging using the erythrocytes as targets (Super-Resolution ultrasound imaging of Erythrocytes (SURE) imaging) is described and investigated. SURE imaging does not require fragile contrast agent bubbles, making it possible to use the maximum allowable mechanical index (MI) for ultrasound scanning for an increased penetration depth. A synthetic aperture (SA) ultrasound sequence was employed with 12 virtual sources (VSs) using a 10-MHz GE L8-18i-D linear array hockey stick probe. The axial resolution was 1.20λ ($185.0\ \mu\text{m}$) and the lateral resolution was 1.50λ ($231.3\ \mu\text{m}$). Field IIpro simulations were conducted on $12.5\text{-}\mu\text{m}$ radius vessel pairs with varying separations. A vessel pair with a separation of $70\ \mu\text{m}$ could be resolved, indicating a SURE image resolution below half a wavelength. A Verasonics research scanner was used for the in vivo experiments to scan the kidneys of Sprague-Dawley rats for up to 46 s to visualize their microvasculature by processing from 0.1 up to 45 s of data for SURE imaging and for 46.8 s for SR imaging with a SonoVue contrast agent. Afterward, the renal vasculature was filled with the ex vivo micro-computed tomography (CT) contrast agent Microfil, excised, and scanned in a micro-CT scanner at both a $22.6\text{-}\mu\text{m}$ voxel size for 11 h and for 20 h in a $5\text{-}\mu\text{m}$ voxel size for validating the SURE images. Comparing the SURE and micro-CT images revealed that vessels with a diameter of $28\ \mu\text{m}$, five times smaller than the ultrasound wavelength, could be detected, and the dense grid of microvessels in the full kidney was shown for scan times between 1 and 10 s. The vessel structure in the cortex was also similar to the SURE and SR images. Fourier ring correlation (FRC) indicated a resolution capability of $29\ \mu\text{m}$. SURE images are acquired in seconds rather than minutes without any patient preparation or contrast injection, making the method translatable to clinical use.

Index Terms—Erythrocytes, fast imaging, micro-computed tomography (CT), microvascular imaging, super-resolution (SR) ultrasound imaging, synthetic aperture (SA), ultrasound localization microscopy (ULM).



Manuscript received 30 April 2024; accepted 4 June 2024. Date of publication 10 June 2024; date of current version 20 August 2024. This work was supported by European Research Council's (ERC) Synergy Grant 854796. (Corresponding author: Jørgen Arendt Jensen.)

This work involved animals in its research. Approval of all ethical and experimental procedures and protocols was granted by the National Animal Experiments Inspectorate under the Ministry of Food, Agriculture and Fisheries of Denmark, under License No. 2020-15-0201-00547, and the Local Veterinarian at University of Copenhagen under Project No. P20-457. The experiments were ethically in accordance with the EU Directive 2010/63/EU for animal experiments.

Please see the Acknowledgment section of this paper for the author affiliations.

This article has supplementary downloadable material available at <https://doi.org/10.1109/TUFFC.2024.3411711>, provided by the authors.

Digital Object Identifier 10.1109/TUFFC.2024.3411711

I. INTRODUCTION

THE last decade has seen the development of super-resolution (SR) ultrasound imaging or ultrasound localization microscopy (ULM).¹ This has resulted in very

¹SR ultrasound imaging has been named with different acronyms based on the various research groups developing the methods. The review by Christensen-Jeffries et al. [1] denotes the general field as Super-Resolution UltraSound (SRUS) imaging. The specific methods have been denoted SR ultrasound imaging (SRI) in [2] and ULM in [3]. We have here selected ULM as an acronym for methods based on injecting gas-filled microbubbles (MBs) intravenously and tracking the scattered signal from the bubbles [1], [3], [4], [5], [6], [7], [8].

Highlights

- SURE imaging uses erythrocytes as targets for fast SR imaging on the exposed kidney on a Sprague-Dawley rat showing the cortical region from SA data acquired with a 10-MHz probe.
- Full transmit voltage was used and processing included beamforming, motion estimation and correction, SVD echo canceling, and peak detections for peak density image visualization.
- SR images acquired in 1–5 s with a resolution between 29 and 70 μm , showing vessels with a diameter down to 28 μm .

high-resolution images of the vasculature, which are beyond the diffraction limit of ultrasound, and allows visualizing vessels with diameters down to 8–30 μm . ULM has, for example, been used in a mouse ear [7], the rat brain [3], rat kidneys [9], human cancers [10], and the human brain [11] for studying the microvasculature. Microvascular imaging has the potential to reveal crucial new information in the study of, e.g., cancer, diabetes, and other vascular diseases.

The bubble density must be sparse in ULM to enable tracking of individual bubbles to create a microvascular flow image from the accumulated tracks [12]. This necessitates a long acquisition time from 30 s to several minutes to allow enough bubbles through the full circulation and to attain a reliable vessel image. This is a substantial problem, as the image resolution is in the micrometer range. Therefore, the probe and patient have to be co-registered with micrometer precision, which can be difficult due to both voluntary and involuntary movements from, e.g., bowels, respiration, and heart beating during the minutes of acquisition.

These problems are sought solved by motion correction of the acquired data [2], [13], [14], [15], [16], [17], [18], but as most of the current methods are in two dimensions, they cannot compensate out-of-plane motion. Also, large motions over time can give problems. The long acquisition times also preclude a real-time display of the ULM and result in very large datasets, which have to be processed offline. Another problem is the fragile ultrasound contrast agents, which burst if exposed to a large acoustic pressure. The scan sequences employed are therefore limited to a mechanical index (MI) of 0.05–0.2, well below current FDA limits of 1.9. The acoustic output is, thus, severely restricted, which limits transmitted energy, and thereby signal-to-noise ratio and penetration depth.

These problems can be solved, if the use of contrast agents can be avoided. This article suggests using the erythrocytes as targets, thus enabling SURE. As the erythrocytes are responsible for transportation of oxygen, they are abundant in circulation with roughly 5 million cells/ mm^3 , and they perfuse any living tissue. They can also withstand the acoustic pressure of clinical ultrasound scanners, and therefore, the full MI range can be employed. Other research groups have also suggested using the erythrocytes as targets instead of ultrasound contrast agents. Park et al. [19] used a deep learning approach trained on simulated data. Motion was estimated but not compensated for in the processing, and high motion frames were only discarded. An 18-MHz probe was employed with a wavelength of 86 μm , and the smallest resolution attained was 65.6

μm , slightly above the diffraction limit of $\lambda/2$. Also, parallel vessels closer than $\lambda/2$ were not shown. Bar-Zion et al. [20] used velocity processing in many frequency bands to separate out the vessels and their direction to enable SR imaging without contrast agents. Three minutes of data was necessary for making the flow filtration, and it was assumed that the vessels did not move in the image, thus neglecting tissue motion. Also, parallel vessels closer than $\lambda/2$ were not shown. Finally, You et al. [21] have also very recently shown a deep learning SR pipeline trained on ULM data from the same view. Here, a 20-MHz probe with a wavelength of 77 μm was used. Fourier ring correlation (FRC) was used to determine the attained resolution of 34 μm , just below the diffraction limit. No motion correction seems to have been included in the processing.

The SURE approach presented here detects the peaks in the speckle pattern after echo canceling and creates the SR image from these interpolated peak positions. The pipeline includes motion correction of the beamformed radio frequency (RF) signals before echo canceling, and it is shown that significant tissue motion from breathing and the heart can be compensated for. The SURE images are also compared to both SR images with contrast agents, simulations, phantoms, and independent micro-computed tomography (CT) scans with a voxel size of 5 μm .

The theory and hypothesis of the approach is described in Section II. Earlier versions of the approach have also been presented in [22] and [23]. This article gives a comprehensive introduction to the method and uses a new scanning sequence, and more results for multiple rats are presented. This article describes and evaluates the vessel density SURE images from the pipeline. The accompanying paper [24] describes how recursive synthetic aperture (SA) imaging and tracking makes it possible to estimate and visualize the blood velocity vector.

The super-resolved image of the microcirculation is attained by acquiring ultrasound data using an SA ultrasound sequence implemented on a Verasonics research scanner as described in Section III-A. A processing pipeline, described in Section III-B, is employed to compensate for tissue motion and remove the tissue signal to yield the erythrocyte signal. Individual cells are not detectable at the current ultrasound resolution, and a speckle pattern will be observed in the vessels. Detecting the peaks in this pattern yields positions inside the vessel, and accumulating these peak positions in the SURE image visualizes the vasculature, which is demonstrated through simulations of small adjacent vessels in Section IV.

In addition, the exposed Sprague-Dawley rat kidney is used as an in vivo model for SURE, followed by ex vivo microvascular micro-CT to yield a vascular reference image for comparison and validation.

II. THEORY AND SURE IMAGING HYPOTHESIS

The image formation in ultrasound can be described by a linear model [25], where $p_r(\vec{r}_2, t)$ is the received signal after beamforming

$$p_r(\vec{r}_2, t) = v_{pe}(t) \star_t f_m(\vec{r}_1) \star_r h_{pe}(\vec{r}_1, \vec{r}_2, t) \quad (1)$$

in which \star_r denotes spatial convolution, \vec{r}_1 is the position of the scatterers, and \vec{r}_2 is the position of the transducer. Equation (1) consists of three distinct terms: v_{pe} is the electromechanical pulse-echo impulse response, which encompasses transducer excitation and electromechanical impulse response during emission and reception. f_m describes the scattering inhomogeneities in tissue due to density and propagation velocity perturbations yielding the scattered signal. h_{pe} is the pulse-echo spatial impulse response relating transducer geometry to the spatial extent of the scattered field. It is the spatial impulse response for the transmitting aperture, including beamforming convolved with the spatial impulse response for the receiving aperture, including beamforming.

The term that should be displayed in medical ultrasound is $f_m(\vec{r}_1)$, which is the scattering by the imaged object. The displayed image is a time and spatially smoothed version, which obscures the finer details in the resulting image. The smoothing consists of a convolution in time with a 1-D pulse $v_{pe}(t)$ and a spatial convolution with a spatially varying $h_{pe}(\vec{r}_1, \vec{r}_2, t)$, which combined corresponds to the point spread function (PSF) of the ultrasound system. A derivation of this model can be found in [25].

Employing SA imaging [26] makes it possible to have a spatially invariant PSF in the imaging plane, where the F-number can be maintained constant within the imaging region. The resulting image is therefore a convolution between the random scatterers and the PSF. The PSF will be approximately Gaussian with an elliptical shape with a maximum at the scatterer's center location, provided that SA imaging is conducted with dynamic apodization in both transmit and receive based on a constant F-number. This is also the underlying assumption of ULM that the PSF has one unique peak for a single MB.

The basic hypothesis underlying SURE imaging is that a random collection of scatterers convolved with the PSF on average will have a peak value within the spatial region of the scatterers. Accumulating a large number of peaks will then yield an image of the underlying vasculature. It is also assumed that the scattered signal is slowly varying when fast imaging is employed, so that the peak position can be tracked over short time periods for vector velocity determination as shown in the accompanying paper [24].

Ultrasound images contain scattering from the stationary tissue and the flowing blood. The scattering from blood is predominantly from the erythrocytes with more than 15 000 cells

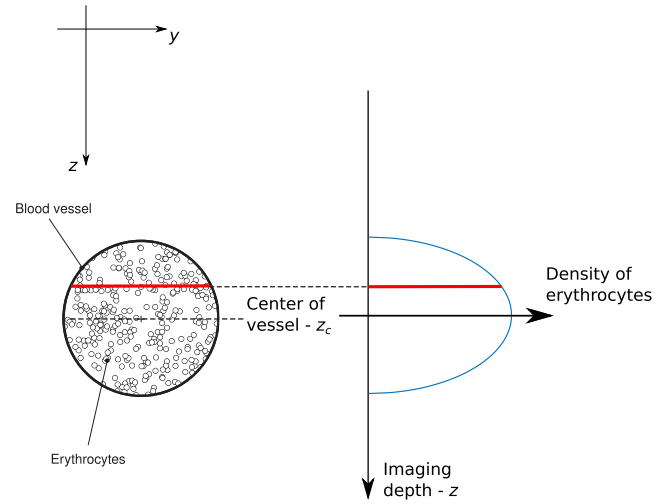


Fig. 1. Geometry for calculating the density of erythrocytes in a small vessel. The vessel is shown in the zy plane, and imaging is conducted in the orthogonal xz plane. It is assumed that the ultrasound field intensity is uniform across the vessel and that the density of erythrocytes is uniform inside the vessel. The number of erythrocytes for a given depth z is then given by the red path length inside the vessel at z .

within the typical PSF, and even probing a single arteriole with a diameter of $50 \mu\text{m}$ will entail probing more than 1300 erythrocytes. To reveal the vasculature, the strong tissue signal has to be removed before the peak positions in the vessels can be detected. This is performed here by first estimating tissue motion and compensating for it to align all the images. The mean image across time will then yield the tissue signal, which ideally can be removed by subtracting the mean image from the images or equivalently making echo canceling on the motion-aligned images using a high-pass filter along imaging time. Often, the tissue cannot be perfectly aligned due to out-of-plane motion, and singular value decomposition (SVD) echo canceling can instead separate the flow signals from the tissue signal by discarding the largest singular values.

After successful echo canceling, only the flow signals are left, and accumulating peak positions in this speckle signal reveals the vasculature. The number of peaks and their positions reflect the density of erythrocytes in the vessels, and the hypothesis can be tested by comparing the density of detections to the theoretical density for a vessel.

The imaging situation for calculating the scatterer density is shown in Fig. 1. The cross section of the vessel is shown in the zy plane, and the SURE imaging is conducted in the xz plane. Assuming that the single vessel is circular and it has a uniform density of erythrocytes inside, the density of SURE detections is proportional to the relative path length $2y/2R$ inside the vessel at the position $z - z_c$ given by

$$P(z) = \frac{2y(z - z_c)}{2R}$$

$$z - z_c = R \cos(\theta), \quad y = R \sin(\theta)$$

$$\theta(z - z_c) = \arccos\left(\frac{z - z_c}{R}\right)$$

giving

$$P(z) = \sin\left(\arccos\left(\frac{z - z_c}{R}\right)\right), \text{ for } |z - z_c| < R \quad (2)$$

where z is the imaging depth, R is the radius of the vessel, and z_c is the vessel center depth position. This assumes that the vessel is smaller than the elevation width of the ultrasound beam, and that it is fully inside the ultrasound beam.

The testing of this theory and hypothesis is conducted by comparing the theoretical and estimated densities for simulated flow data for small vessels in Section VII-B and for measurements on a micro-phantom in Section VII-C. The shape and size of the theoretical and estimated density should be the same, and the difference between the densities indicates the uncertainty in the SURE image. The hypothesis can also be tested by comparing the extent of the vessels in the SURE image with the size of vessels in high-resolution micro-CT scans as conducted in Section VII-F.

III. METHODS FOR DATA ACQUISITION AND PROCESSING PIPELINE

This section describes the ultrasound scan sequence, the processing pipeline, and the postprocessing employed to compare SURE, ULM, and micro-CT images.

A. Ultrasound Scan Sequence

The ultrasound data were acquired using a Verasonics Vantage 256 research scanner (Verasonics, Inc., Kirkland, WA, USA) connected to a 168-channel GE L8-18iD (GE HealthCare, Chicago, IL, USA) linear array probe. The 10-MHz probe had a wavelength pitch of $150 \mu\text{m}$. The pulsedwidth modulation transmit stage in the Verasonics scanner yielded a center frequency in tissue of 9.29 MHz and a wavelength of $166 \mu\text{m}$ when estimated from the mean frequency of the received tissue signal's power density spectrum. An SA ultrasound sequence with 12 virtual sources (VSs) evenly spread across the aperture was employed [26]. Each VS had a transmit F-number of -0.7 with the transmit focus placed at a depth of -3.36 mm behind the transducer surface and used 32 elements for the defocused emissions with a Hanning apodization across the active aperture. For the example in Section VII-G, the emissions were repeated in an interleaved imaging scheme with 2×12 VS to make it possible to estimate high blood velocities as described in [27]. The derated MI of the sequence was 0.49 and the derated $I_{\text{spta},3}$ was 4.79 mW/cm^2 for a pulse repetition frequency of 5 kHz. Probe heating was below $9.3 \text{ }^\circ\text{C}$ in free air and $2.1 \text{ }^\circ\text{C}$ on a phantom. Data were sampled at a frequency of 62.5 MHz/14 bits for a duration of up to 46 s with a pulse repetition frequency of 5 kHz resulting in a high-resolution image frame rate of 416.7 Hz for the noninterleaved scan sequence and 208.3 Hz for the interleaved sequence. The data were stored in local RAM and transferred to disk and a computer cluster for later processing.

B. Processing Pipeline

The acquired data were processed using the SURE pipeline shown in Fig. 2, where each box describes a processing stage. Examples of the resulting images are shown below the processing boxes. All processing was conducted in MATLAB (MathWorks, Natick, MA, USA) with processing modules developed specifically for SURE imaging. The stored data were beamformed using the graphics processing unit (GPU) code presented in [28] with an axial sampling density of $\Delta z = 10.4 \mu\text{m} = \lambda/16$ and a lateral density of $\Delta x = 41.5 \mu\text{m} = \lambda/4$, where λ is the estimated ultrasound wavelength of $166 \mu\text{m}$ in tissue. Dynamic focusing was employed in transmit and receive with an F-number of 0.7, and Hanning apodization on the receiving elements and among virtual transmit sources was dynamically calculated from the F-number to maintain a uniform resolution across the imaging depths. This yielded images with 1871 RF samples for a depth range of 5–23 mm and 655 image lines for a 25.2-mm image width.

1) *Tissue Motion Estimation With Speckle Tracking*: Tissue motion was estimated from the envelope data using speckle correlation [29] similar to the approach used in [2] for determining both the axial and the lateral components with a precision in the micrometer range. The tenth frame in the sequence is selected as the reference frame for the motion estimation.

2) *Tissue Motion Estimation With Transverse Oscillation*: Transverse oscillation (TO) motion estimation was also implemented to make the processing significantly faster [30], [31]. The lateral oscillation period was controlled by filtering the RF data to introduce the lateral oscillation, and the estimator in [31] was used for motion estimation. The motion estimates were calculated using a matrix formulation, and the estimates were smoothed over a $2 \times 2 \text{ mm}$ region to increase precision. The TO period was estimated from the lateral frequency in the actual data after filtration and the estimated wavelength was used during the motion estimation. This method enables a real-time implementation of the SURE pipeline on a standard GPU [32].

3) *Tissue Motion Correction*: The RF images were then motion compensated to align them with the reference image as

$$y_c(k, j, i) = y(k - r_{kms}(k, j, i), j - r_{jms}(k, j, i), i) \quad (3)$$

where the image values for subpixel positions were found through 2-D spline interpolation. Here, $r_{kms}(k, j, i)$ is the spline interpolated motion at position (k, j) for the i th frame in the axial direction and $r_{jms}(k, j, i)$ is in the lateral direction.

4) *Tissue Signal Removal*: The tissue signal was removed from the spatially aligned images using the SVD processing method [33], [34] to enhance the flow signal from the erythrocytes. The Casarotti matrix C_s was formed from the data and had a size of $N_z N_x \times N_t$, where N_z is the number of samples in the axial direction, N_x is the number of lateral lines, and N_t is the number of time samples (frames). The SVD was then performed on C_s . The tissue signal was contained in the first N_{tissue} singular values, which were set to zero. Singular values above N_{noise} mostly contained noise and were

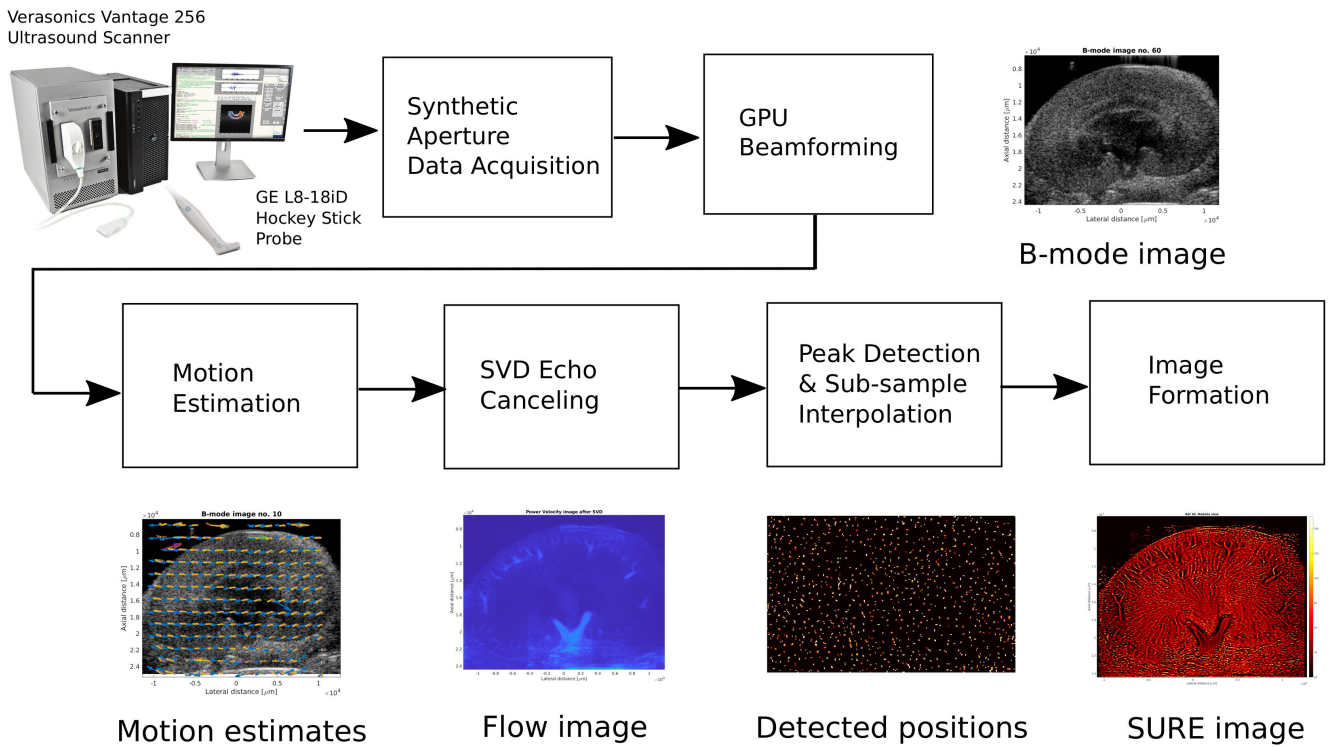


Fig. 2. Processing stages in the SURE pipeline. The various processing blocks are shown in the middle row and examples of the resulting images are shown next. From left to right, data are acquired with an SA ultrasound sequence using a Verasonics Vantage 256 scanner and a GE L8-18iD linear “hockey stick” probe. They are beamformed offline on a GPU card, and the motion vector field is found using the envelope signal. The images are spatially aligned, and the stationary signal is removed using SVD processing. Local peaks in the remaining signal are found, and subpixel interpolation of peak positions is conducted. The SURE image is produced by accumulating the positions of all the peaks in all frames. Image of scanner used by permission of Verasonics.

also removed in the processing. The Casarotti flow matrix was then reconstructed from the remaining singular values [35].

The determination of N_{tissue} and N_{noise} is closely linked to the used imaging sequence, transducer, scanner signal-to-noise ratio, and the detection threshold described next. There are suggestions for automatically determining the two cutoff values [35], but they do not yield consistent results for the various images. The determination of N_{tissue} and N_{noise} was therefore performed manually by processing a subset of the clinical images for various values of the cutoff and the detection threshold, and a fixed set of values giving the image most closely resembling the kidney vasculature was used for all images presented here. They were $N_{\text{tissue}} = 0.1 N_t$ and $N_{\text{noise}} = 0.75 N_t$ for a detection level of -30 dB.

The number of calculations to perform for one decomposition is proportional to $O((N_z N_x) N_t^2)$, and the Casarotti matrix gets very large for even moderately large images. The image stack was therefore divided into overlapping patches as suggested in [34] of 180×180 pixels and $N_t = 400$ frames for roughly 1 s of data, where a border of 40 pixels overlapped adjacent patches. This corresponds to a patch size of $1872 \times 7470 \mu\text{m}$ (axial \times lateral size).

5) Erythrocyte Detection: The position of unique local peaks in each of the patches was then detected. The envelope data were logarithmically compressed and normalized with respect to the standard deviation (SD) of all the patches in the first image. Peaks above a threshold of -30 dB from the maximum in the first image were detected as erythrocyte locations,

and the subsample location of each peak was found from a polynomial interpolation around the peak position. Detections outside of the 100×100 pixels central core of the patch were removed, and only detections inside the central region were kept to avoid edge artifacts in the image. This was performed for all patches and all frames in the sequence, resulting in a list of detected positions with subpixel precision.

6) Image Display: Finally, the SURE images were constructed by accumulating all detected positions in an image with a pixel size of $2 \times 2 \mu\text{m}$. The images were smoothed with a Gaussian low-pass kernel

$$h(k, j) = \exp - \frac{(k \Delta z)^2}{2\sigma_z^2} \exp - \frac{(j \Delta x)^2}{2\sigma_x^2} \quad (4)$$

with SDs $\sigma_z = 4 \mu\text{m}$ (axial) and $\sigma_x = 15 \mu\text{m}$ (lateral) to account for inaccuracies in the motion estimation, subsample registration, and sparseness of detection. These images show the density of detections and correspond to places in the images with flow.

C. Co-Registration and Micro-CT Maximum Intensity Projection

The micro-CT slice corresponding to the SURE image was resampled and stored on a rectangular field-of-view (FOV) (axial, lateral, and elevation) $[18.04 \times 23.54 \times 0.900]$ mm with a voxel spacing of $[1 \times 3.8 \times 900] \mu\text{m}$. The set of micro-CT slices that correspond to the SURE image was then manually

TABLE I

SIMULATED PHANTOM PROPERTIES FOR THE TUBE PAIRS. THE VESSEL CENTER IS THE DEPTH FOR THE FIRST TUBE PAIR. TUBE SEPARATION IS DISTANCE BETWEEN TUBE CENTERS, AND FLOW DIRECTION INDICATES WHETHER FLOW IS OPPOSITE IN EACH TUBE OR IN THE SAME DIRECTION. THE RADIUS OF ALL TUBES IS $12.5 \mu\text{m}$

Vessel center depth mm	Tube separation μm	Lateral velocity mm/s	Flow direction
7.000	150	+10 & -10	opposite
7.500	150	+10	right
8.100	100	+10 & -10	opposite
8.500	100	+10	right
9.075	70	+10 & -10	opposite
9.500	70	+10	right
10.000	50	+10 & -10	opposite
10.400	50	+10	right

found using the program ITK-SNAP [36]. An overall good fit could be obtained allowing only translations, rotations, and small amounts of scaling.

A grid of sample points spanning the same SURE FOV, but with grid point spacing $[1 \times 3.8 \times 22.6] \mu\text{m}^3$, was generated and transformed to the location of the SURE/micro-CT overlap using the transformation parameters of the co-registration. The intensity of the micro-CT volume was sampled at each grid point using linear interpolation. A local maximum intensity projection (MIP) was made by taking the maximum sampled intensity in the “elevation” direction of the grid points. This represents the ground truth vasculature within a volume similar to the one in which the SURE image was acquired.

A smaller part of the kidney cortex was scanned with a $5\text{-}\mu\text{m}$ voxel size to attain a higher resolution to compare part of the SURE image with.

IV. SIMULATIONS FOR VALIDATION

The SURE processing method was validated using Field II simulations [37], [38] using the Pro version [39]. Point scatterers were simulated to reveal the resolution of the imaging sequence. A simulated phantom mimicking flow in arterioles and venules was made with the properties shown in Table I. The SA scan sequence with 12 VSs for the in vivo data acquisition was simulated using the impulse response and geometry of the 168-element GE L8-18iD linear array probe employed for the measurements. The flow tubes had a radius of $12.5 \mu\text{m}$ and contained a parabolic, laminar flow profile with a speed of $\pm 10 \text{ mm/s}$. Eight tube pairs with opposite or unidirectional flow were simulated with properties shown in Table I. The scatterer density was in the first simulation 750 scatterers per λ^3 at a 10-MHz frequency to ensure fully developed speckle patterns. In human blood at a hematocrit of 45%, there is roughly 4.5×10^6 red blood cells per mm^3 [40], giving 15200 cells in a volume of λ^3 and a mean distance of $6.1 \mu\text{m}$ between individual cells. The simulation had a mean distance between scatterers of $16.5 \mu\text{m}$. Thus, the density was lower in the simulation, but still with a mean scattering distance significantly below the wavelength

of $166 \mu\text{m}$. A second simulation with 11455 scatterers per λ^3 was conducted to prove that the same results were obtained with both scatterer densities.

V. MICRO-PHANTOM EXPERIMENTS

A micro-phantom has been fabricated by 3-D printing of a PEGDA 700-g/mol hydrogel using stereolithography and its geometry and the setup is shown in Fig. 3. The phantom measures $20.0 \times 12 \times 12 \text{ mm}$, and the voxel size of the printer is $(\Delta x, \Delta y, \Delta z) = 10.8 \times 10.8 \times 20 \mu\text{m}$. More information about the fabrication process can be found in [41]. The flow micro-phantom contains a single cylindrical $100\text{-}\mu\text{m}$ radius channel placed 3 mm from the top surface of the phantom. The channel was folded to give parallel tubes with channel center separations from 300 to $260 \mu\text{m}$ and wall-to-wall distances of 100 to $60 \mu\text{m}$. The flow channel was infused at $0.1 \mu\text{L/s}$ with SonoVue (Bracco, Milan, Italy) in a 1:1 dilution giving a peak velocity of 6.3 mm/s . The contrast agent was used due to its availability, ease of use, and comparability with the phantom. Other commercial Doppler fluids tend to clog the phantom, where SonoVue makes it possible to reuse the phantom several times.

VI. ANIMAL EXPERIMENTS

A. Animal Preparation

The experiments were conducted on four healthy male Sprague-Dawley rats (body weight: 329–382 g, Janvier Labs, Le Genest-Saint-Isle, France). The procedures were executed at the University of Copenhagen with respect to all local ethical standards and performed according to protocols approved by the Danish National Animal Experiments Inspectorate. The ethical policy of the University of Copenhagen is consistent with that of the EU Directive 2010/63/EU for animal experiments. The rats were housed in an animal facility at the Department of Experimental Medicine, University of Copenhagen, under the responsibility of trained animal caretakers. The rats were fed standard laboratory chow (13198 FORTI) ad libitum and allowed free access to water.

The SURE imaging was performed on anesthetized rats after laparotomy. The rats were anesthetized in a chamber with 5% isoflurane delivered in 65% nitrogen and 35% oxygen. The anesthesia was maintained with an isoflurane concentration of 1.5%–2%. A tracheostomy was inserted to secure a respiration cycle of 72 respirations/min through a mechanical ventilator (Ugo Basile, Gemonio, Italy). The arterial blood pressure was measured continuously by a Statham P23-dB pressure transducer (Gould, Oxnard, CA, USA) through a polyethylene catheter (PE-50) in the left carotid artery. The left jugular vein was catheterized with a polyethylene catheter (PE-10) for continuous infusion of $20\text{-}\mu\text{L/min}$ Nimbex (cisatracurium, 0.85 mg/mL, GlaxoSmithKline, Brentford, U.K.). The rats were placed in the supine position on a heating table to maintain normal body temperature ($37 \text{ }^\circ\text{C}$). After laparotomy, a metal retractor under the left diaphragm pulling slightly cranially was established. This made it possible to further expose the left kidney and reduce the respiratory motion.

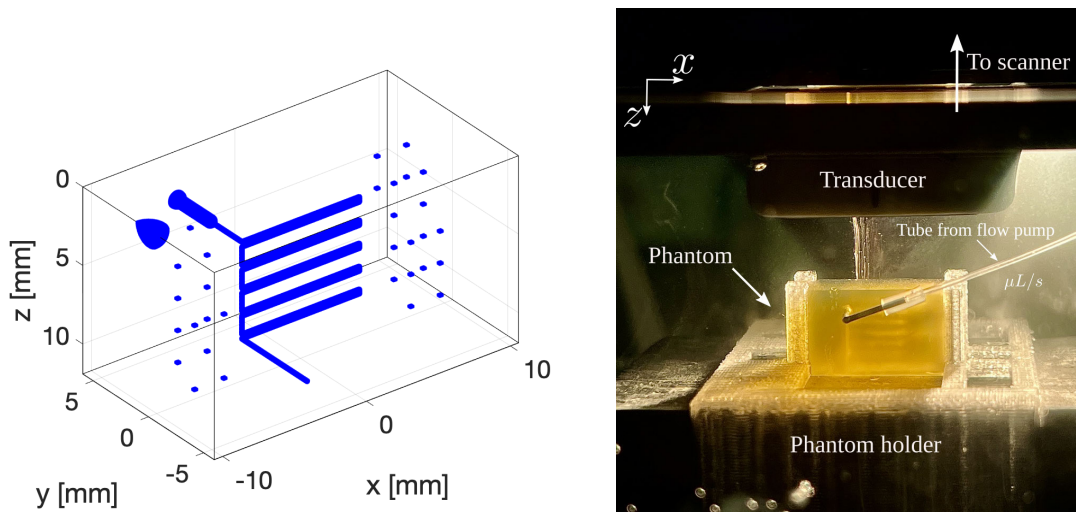


Fig. 3. Drawing of the 3-D printed micro-phantom (left). The blue indicates the 3-D printed structures inside the phantom, which consists of small fiducial markers and the convoluted flow channel with parallel tubes. On the right is the measurement setup for the perfusion test, including the 3-D printed phantom, phantom holder, transducer, and tube from the flow pump.

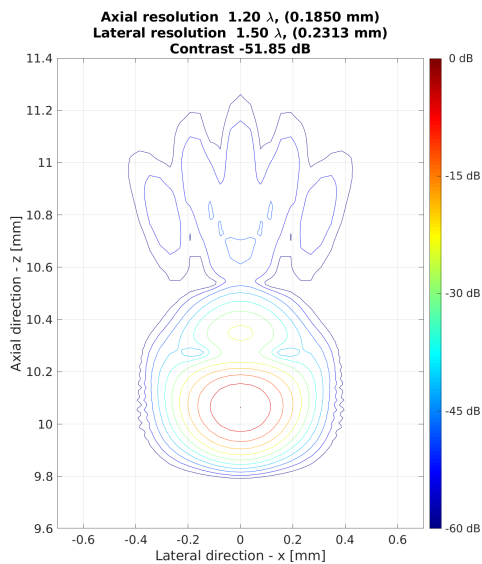


Fig. 4. Simulated PSF of the imaging setup. The axial resolution is 1.20λ (0.1850 mm), and the lateral resolution is 1.50λ (0.2313 mm) with an integrated sidelobe level of -51.85 dB.

B. Ultrasound Scanning

The SURE imaging was performed coronally in two different planes of the kidney to visualize different vessel structures. The guidance of the probe was performed using the B-mode image. First, the probe was placed in the renal center showing the vasa recta (see the top of Fig. 9), and second, it was placed more dorsally to the center showing the large segmental and arcuate arteries and veins (see the bottom of Fig. 11).

C. SR Imaging Experiments

A Sprague-Dawley rat kidney was also scanned with injection of the SonoVue MB contrast agent using exactly the same probe placement and scanner. The MB dilution ratio was 1:5 and the continuous injection flow rate was $55 \mu\text{L}/\text{min}$. The two scans were performed within at most 40 min of each

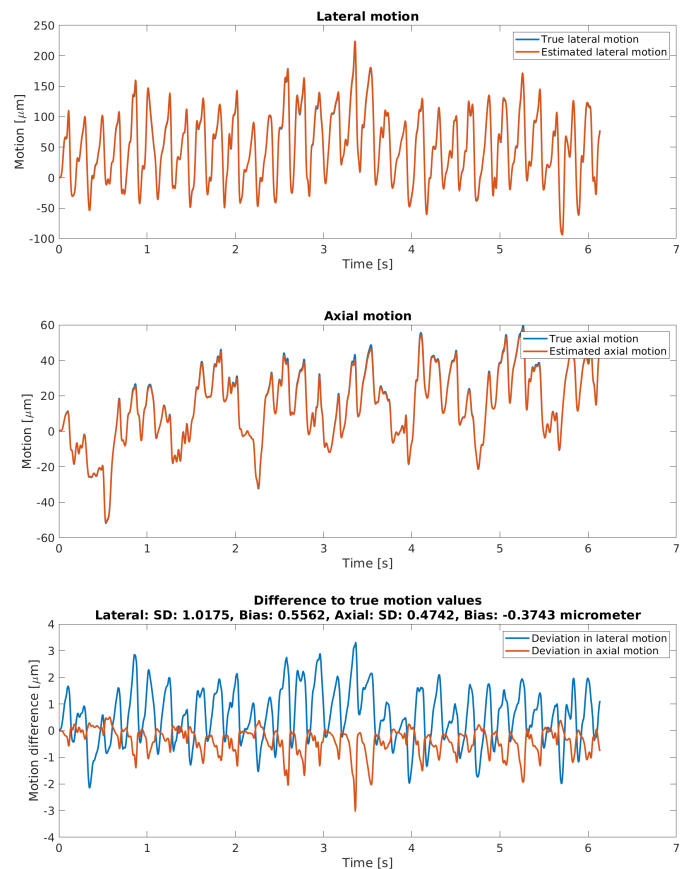


Fig. 5. Estimated tissue motion from the phantom simulation using the TO approach. The top figure shows true and estimated lateral motion, the middle is the axial motion, and the lower graphs show the difference between the two. Note that the y-axis on the three graphs is different.

other to minimize the time between scans and, hence, the potential movement of the kidney. An amplitude modulation scheme was used [42], [43] with three emissions: one with all elements, one with even elements, and one with odd elements. The last two emissions were inverted, so summing all three

emissions gave the nonlinear response. The same 12 VSs as for the SURE imaging and the same probe and scanner were used. The transmit voltage was reduced to 10 V to keep MI low at 0.05. The pulse repetition frequency was 20 kHz between the three emissions and 2 kHz between the 12 VSs. The transmit frequency was 10 MHz for a resulting estimated wavelength of $166 \mu\text{m}$ in the tissue. Data were streamed in real time from the Verasonics scanner to the connected PC as described in [44] making it possible to acquire 160 s of data. Data storage time was around 3 min for 130 GB of data. Motion correction was used as in [2], and a hierarchical Kalman tracking was employed to make track density images [45].

D. Ex Vivo Micro-CT

After SURE imaging, the rats were prepared for the infusion of intravascular micro-CT contrast. Six ligatures were placed to isolate the renal circulation and optimize contrast flow into the kidney: a ligature around the left renal artery, two around the left renal vein, one around the cranial part of the aorta (below the right renal artery but above the left renal artery), and two ligatures around the caudal part of the abdominal aorta to fixate the catheter (PE-50). To prevent blood clots during contrast infusion, the rats were heparinized (Heparin "SAD" 1000 IE/mL, Amgros, Copenhagen, Denmark) with 1000 IE/kg intravenously. The catheter in the abdominal aorta was retrogradely inserted and fixated with the catheter tip just below the left renal artery and the cranially placed ligature around the aorta was tightened. The ligature around the left renal vein closest to the inferior vena cava was closed, and a small hole was made in the vein to allow infused solutions to leave the renal vasculature. The left kidney was perfused with 9 mL preheated (40°C) heparinized saline (1000-IE/mL heparin diluted 1:100 in isotonic saline) at 2 mL/min. Just after initiating the renal vascular flushing, the rats were euthanized by decapitation. When only clear saline was exiting the renal vein, 3-mL Microfil contrast agent (MV122, Flow Tech Inc., Carver, MA, USA) was infused at 1 mL/min. The infusion continued until the entire surface of the kidney was yellow and contrast had left the renal vein. The kidney was left for 60 min allowing contrast curing and then excised, decapsulated, and fixated in formaldehyde. Finally, the kidney was embedded in paraffin in a customized cylinder-shaped holder. The kidneys were scanned for 11 h in a ZEISS XRadia 410 Versa micro-CT scanner (Carl Zeiss Microscopy GmbH, Jena, Germany) with an isotropic voxel size of $22.6 \mu\text{m}$ and the following additional settings: tube voltages of 40 kV, power of 10 W, 0.175-mA current, appertaining LE2 filter, and 360° scan around the vertical axis with 3201 different projections (0.112° rotation steps).

A single rat kidney was also scanned for 20 h in a ZEISS XRadia 410 Versa micro-CT scanner with an isotropic voxel size of $5 \mu\text{m}$ to enhance resolution.

VII. RESULTS

These sections present the resulting SURE images. The simulated images for validation are described in Section VII-B. The micro-phantom experiments in Section VII-C, the in vivo

rat images, and the comparison to micro-CT scans are described in Section VII-D, and finally, the comparison to ULM is given in Section VII-G.

A. Image Resolution

The PSF of the imaging sequence is shown in Fig. 4. The simulation gave an axial resolution of 1.20λ ($185.0 \mu\text{m}$) and the lateral resolution was 1.50λ ($231.3 \mu\text{m}$) with an integrated sidelobe level of -51.85 dB . Here, the theoretical wavelength at 10 MHz has been used. The resolution is 1.08λ and 1.36λ when the estimated wavelength in tissue is used. The point is placed at 10 mm, and the probe size is 25 mm, so the F-number of 0.7 can be maintained in both transmit and receive for this point. This is the ideal resolution of the setup for a fully uniform transducer and a perfect point target. The actual F-number will be somewhat lower due to the reduction of the effective aperture from the Hanning apodization in both transmit and receive. It, thus, indicates that the distance between two targets has to be separated to be isolated in conventional B-mode imaging. Lower F-numbers have been used, but this reduces the contrast in the image, and the F-number of 0.7, thus, gives the best contrast and resolution. This quality PSF can theoretically be maintained down to 17.5 mm, which usually is at the lower part of the image of the scanned kidneys. The simulations reveal contrasts below -50 dB and constant resolutions down to 22 mm, which covers the full kidney.

B. Validation

The tissue motion for the simulated phantom example was estimated using the TO method and is shown in Fig. 5. The lateral wavelength was four axial wavelengths, and the lateral pulse had four oscillations windowed with a Hanning weighting. The RF data were filtered by a pulse with eight oscillations before motion estimation with the autocorrelation estimator [46], and the correlation function was averaged across $2 \times 2 \text{ mm}$. Both precision and accuracy can be calculated, as the true motion is known. For the lateral motion, the SD was $1.02 \mu\text{m}$ and the bias was $0.56 \mu\text{m}$, and for the axial motion, the SD $0.47 \mu\text{m}$ and the bias was $-0.37 \mu\text{m}$. The wavelength was $166 \mu\text{m}$.

The various images from the simulation of the microtubes described in Section IV are shown in Fig. 6. The simulated B-mode image for the eight tube pairs and the high-density scatterer simulation is shown on the top image before echo canceling and below after SVD echo canceling. The tube pairs can barely be discerned and only the top tube pair can be separated, whereas the lower pairs are not seen as two tubes. The power Doppler image is displayed below showing that flow in the tubes is detected, but only the top pairs of tubes are clearly separable. Applying the SURE pipeline on the data gives the middle image for 3 s of data. The top six tube pairs can be separated in the image at this zoom level. The lowest graph shows the SURE image summed across all lateral positions, which is then normalized by the maximum value for showing the relative density of detections in black along with the peak values separation. The theoretical values

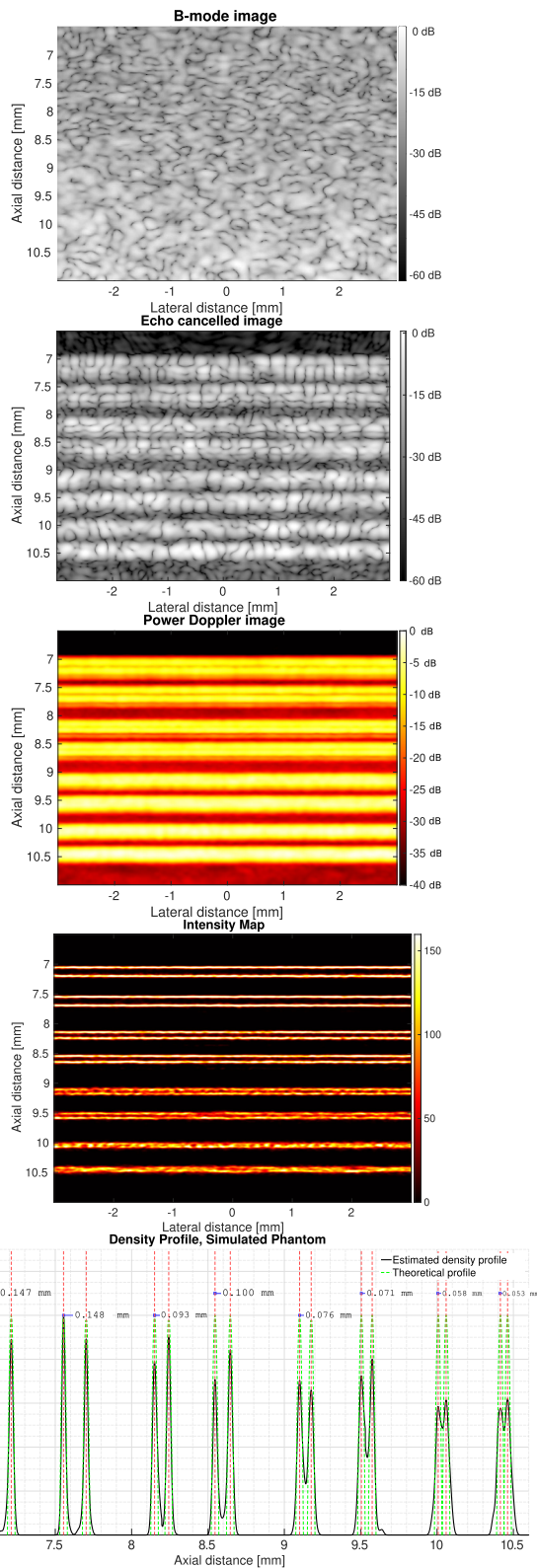


Fig. 6. Simulated flow in eight tube pairs for both opposite and same direction flow. The top graph shows the B-mode image, the echo canceled B-mode image, and the corresponding power Doppler image followed by the processed SURE image. The bottom graph shows the quantification of the detection and resolution capabilities of the SURE processing. The black line is the laterally summed SURE density image, and the green curves are the theoretical values. The Supplementary Material contains the echo canceled B-mode video shown on the top in FieldII_simulated_phantom_SVD_echo_canceled.mp4.

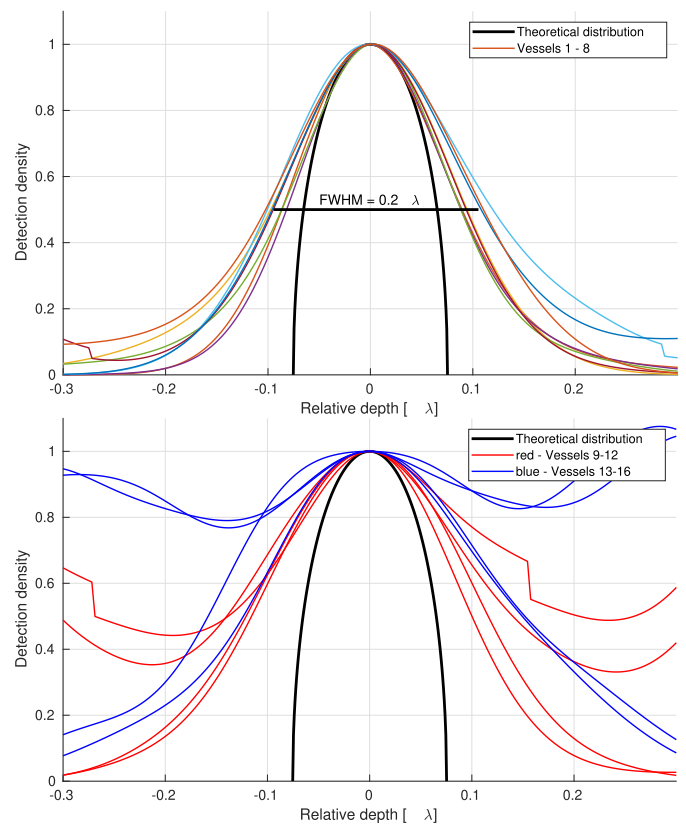


Fig. 7. Individual density profiles for the first eight simulated tubes (top) and the remaining tubes (bottom). The thick black curve is the theoretical density curve, and the other curves are the laterally summed SURE density image.

given by (2) for the true vessel positions are shown as the green profiles in the lower graph in Fig. 6. The positions of the various tubes are determined correctly within $6 \mu\text{m}$ of uncertainty for the separable vessel pairs, and the uncertainty is $8 \mu\text{m}$ for the vessel pair with a $50\text{-}\mu\text{m}$ separation between centers and $25 \mu\text{m}$ between vessel edges. The lower density simulation gave similar results with uncertainties of 5 and $10 \mu\text{m}$. These figures should be compared with the wavelength of the ultrasound probe, which at its center frequency of 9.29 MHz is $166 \mu\text{m}$, so tubes closer than half a wavelength can be separated in SURE imaging. The SURE density profiles for the first top eight isolated vessels are shown in Fig. 7 on top of the theoretical density for this simulation. The simulated SURE image closely follows the theoretical density from (2) until $\pm 0.1\lambda$ for a density value above 0.6, after which it widens to around $\pm 0.2\lambda$ at the base. The full-width at half-maximum (FWHM) is 0.2λ compared to the estimated wavelength, and the density profiles are, thus, 34.2% wider than the actual $25\text{-}\mu\text{m}$ size of the vessel. The similar curves for vessels 13–16 are shown in the bottom graph in Fig. 7. The adjacent vessels widen the density function, and the vessels are depicted wider than they are. For vessels closer than $\lambda/3$, the density is quite distorted. This can be alleviated by employing the estimated flow direction as described in [24].

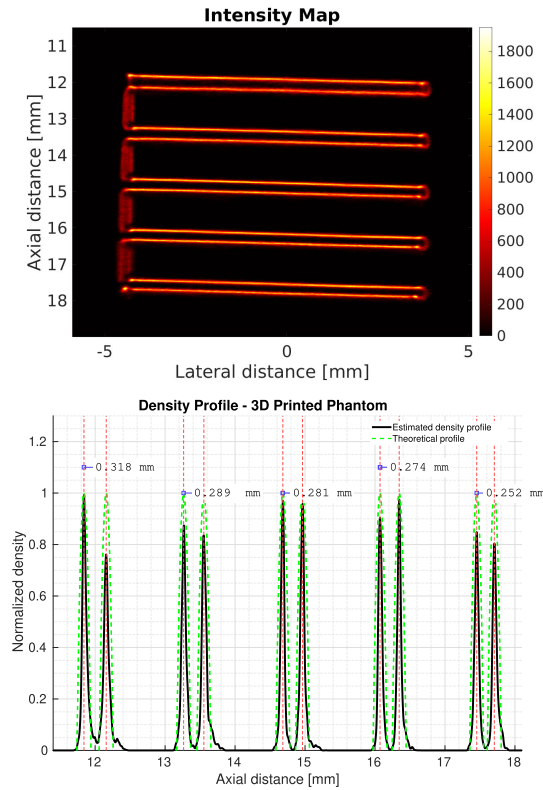


Fig. 8. Top image shows the SURE density image of flow in the 3-D printed micro-phantom for five pairs of vessels. The color bar shows the number of detections per pixel. The bottom graph shows the probability density for the various vessels as the solid line, and the green dashed line shows the theoretical probability density function.

C. Micro-Phantom Experiments

The SURE image for the 3-D printed micro-phantom experiment is shown in the top image in Fig. 8. The five pairs of parallel channels are all visualized, can easily be separated, and only show scatterers inside the flow channels. The corresponding probability density functions are shown as the black solid line next. The theoretical density functions as given by (2) are shown as the green dashed line with the distance between vessel centers on top. The designed vessel centers in the phantom are from 300 to 260 μm with a decrease of 10 μm per vessel pair and a print resolution of 10.8 μm . The wall-to-wall distance in the final vessel pair is 60 μm corresponding to 0.36λ .

D. In Vivo SURE Examples

An example of an SURE image of the left kidney of a Sprague-Dawley rat is shown in Fig. 9. The scan was conducted over 24 s for acquiring 10 000 images. The pipeline detected 41 574 604 peaks in total for a mean detection of 4157 peaks/image. The bottom-left image shows the normal anatomic B-mode image, the top image is the SURE image, and the bottom-right image shows the corresponding micro-CT image. The SURE image displays the very high density of vessels throughout the kidney.

In Fig. 10, two 2×2 mm enlarged areas of the SURE image show the details of the renal arcuate vessels closely surrounded

TABLE II

REPEATED MEASUREMENTS OF THE FOUR VESSEL SIZES IN THE LEFT IMAGE IN Fig. 12. THE ACQUIRED SURE DATA HAS BEEN SPLIT INTO FOUR INDEPENDENT MEASUREMENTS OF 6 s, AND THE VESSEL SIZE HAS BEEN AUTOMATICALLY DETERMINED FOR THE FOUR DATASETS

Peak number	Mean size μm	SD of size μm
1	59.3	4.0
2	89.3	12.6
3	78.1	14.7
4	68.0	13.7

by a dense mask of smaller vessels. Two different scanning planes in a second rat kidney are shown in Fig. 11, with the SURE images on the left and the corresponding micro-CT images in the middle. The top-left SURE image shows a coronal image slice down the center of the kidney, revealing the renal medulla encircled by the cortex with roughly the same view in the micro-CT image in the middle. The SURE image depicts the long straight vasa recta bundles of the medulla in which the individual vessels have a diameter of $\approx 20 \mu\text{m}$. The individual vasa recta vessels are not separated but are shown like vessel structures, which are a bundle of several vessels, but the general direction and position of the bundles are visualized. Paired arcuate arteries and veins are also visible on the border between the cortex and medulla. The same structures are found in the micro-CT image in the middle and the fused image to the right visualizes the correspondence between the two images. The bottom-left SURE image includes some of the major segmental and arcuate vessels in the kidney. Again, a clear correspondence between structures in the micro-CT and the SURE images is seen in the fused image on the bottom right.

Quantification of vessel sizes from zoomed images from Fig. 9 is shown in Fig. 12. The relative number of detections is calculated across the white lines. For the full 24-s collection of data, vessels with a diameter down to 28 μm are clearly detected and separated from the background flow. The data can be sectioned into four datasets of 6 s, which are fully independent. Making the SURE image for each of these four datasets and performing the same quantification for all four vessels gives mean sizes with SDs, as shown in Table II. Even though only a fourth of the data is used (6 s), all four vessels are still reliably detected and the mean SD of all size estimates is 12.0 μm .

The time evolution of the SURE image is illustrated in Fig. 13. The top-left image is made after 0.1 s. The major vessels are depicted, and it can be seen that flow is present in the entire kidney, but the smaller vessels with diameters below 100 μm are barely visible. This improves progressively when information from more frames is added. The middle top row is after 0.2 s and the right top image is after 1 s of data. The vessels in the cortex with a diameter of 100 μm are now clearly discernible, and all vessels are clearly visible. Only marginal improvement is seen when adding data for 5–20 s. A video of the time evolution of the SURE image

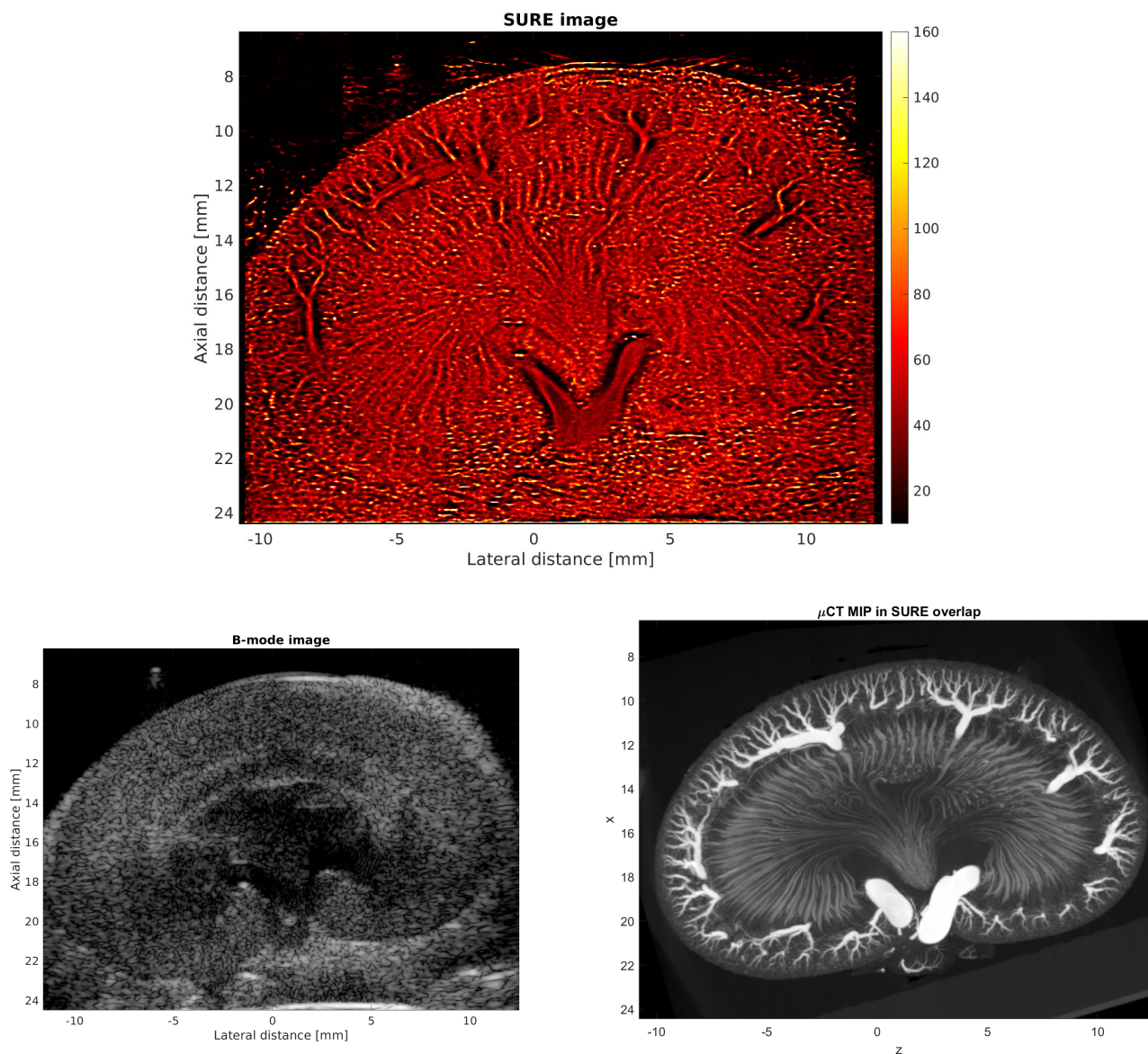


Fig. 9. Images of the vascular tree of the left rat kidney. The bottom left is the B-mode image showing the anatomical structures of the kidney, and the top is the SURE image showing the vascular tree in the anesthetized rat. The corresponding micro-CT image obtained ex vivo of the same kidney is shown on the bottom right (a voxel size of $22.6 \mu\text{m}$).

can be found in the Supplementary Material (video file: [sure_rat_59_real_time_2023.09.01.mp4](#)).

E. Fourier Ring Correlation

Another method for estimating resolution is by using FRC, where data from two images are correlated, and the resolution is determined from the correlation [47], [48], [49]. The data for the image in Fig. 9 are split into two, and two images are made as shown in Fig. 14, where the top-left image is for the first 12 s of data and the second is for the remaining 12 s. The FRC is then calculated and smoothed with a low-pass filter to reduce noise. Bit-based information threshold curves are used for the resolution threshold level as described in [50]. The result is shown in the graph in Fig. 14 together with the threshold curves for 0.5- and 1-bit resolution. The resolution

is $29.1 \mu\text{m}$ for the 0.5-bit threshold and $40.2 \mu\text{m}$ for the 1-bit threshold.

F. Consistency

The correspondence and consistency of the SURE image compared with a micro-CT scan are shown in Fig. 15. Here, the SURE image on the left has been processed for 3 s and the -6-dB size of the vessel determined. A micro-CT scan with a voxel size of $5 \mu\text{m}$ has been performed on the removed kidney filled with the contrast agent Microfill and scanned for 20 h for this part of the kidney. The vessel size was determined by making the MIP across 400 CT slices (2-mm slice thickness) and then count the number of bright pixels across the vessel lumen. The quantitative number is also shown in Fig. 16. Here, the SD of the SURE vessel size has been determined by

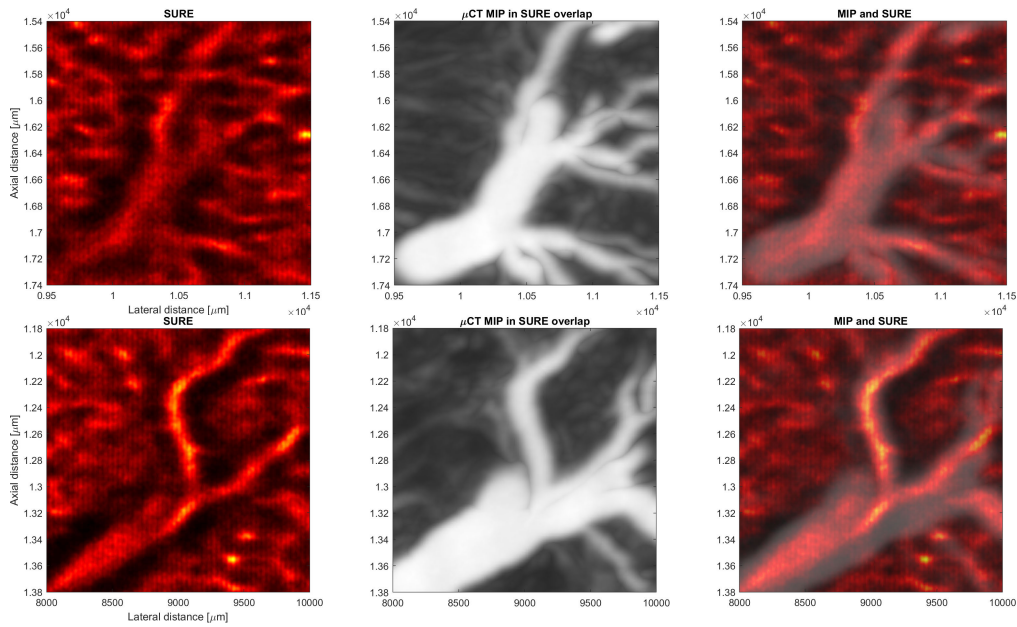


Fig. 10. Enlargement of details of the vasculature in the SURE image shown in Fig. 9 (center). Branching of the arcuate arteries is visible as is the surrounding vascular network. The left column shows the SURE images, the middle column shows the micro-CT images (a voxel size of $22.6 \mu\text{m}$), and the two are fused in the right column.

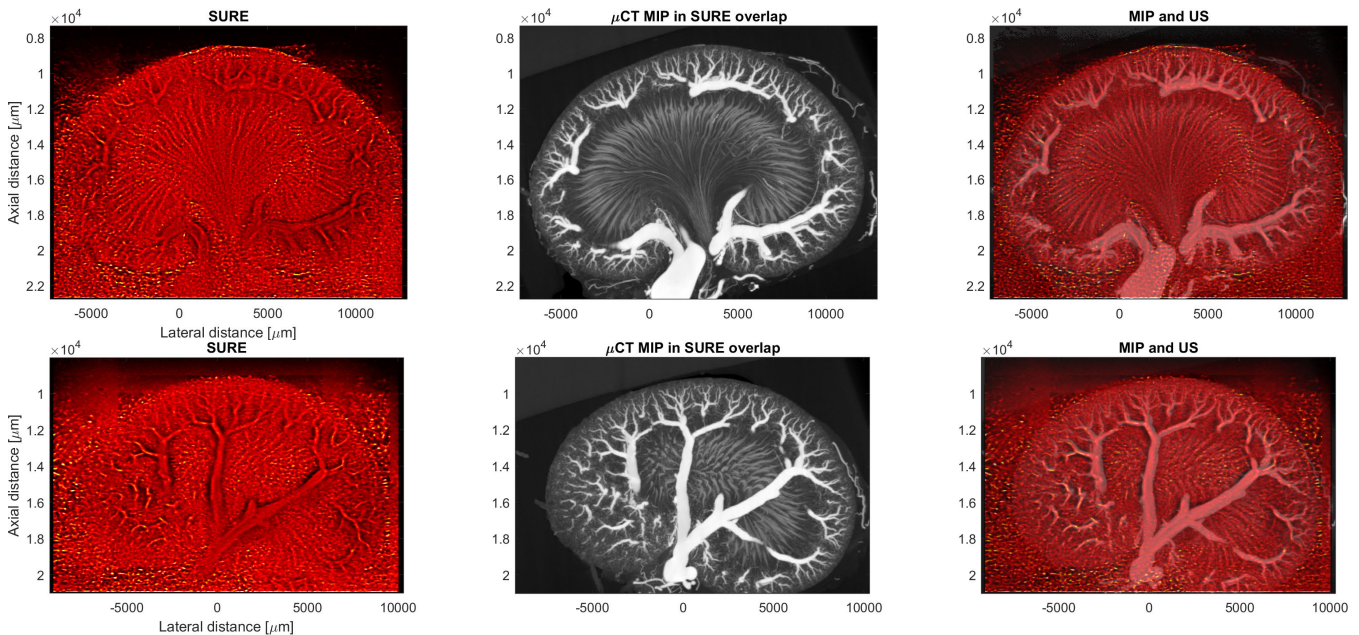



Fig. 11. Examples of SURE images (left) and corresponding micro-CT images (center, a voxel size of $22.6 \mu\text{m}$) for two different scanning planes of a rat kidney. The images are fused on the right. The top images show the central part of the kidney where long straight vasa recta extend from the outer medulla (just below the cortical part to the innermost part of the papilla). Horizontal arcuate vessels branch into smaller cortical radial vessels extending toward the kidney surface. The bottom images show a view of the large segmental and arcuate vessels for the same kidney. Notice the correspondence in structure between the SURE images and the micro-CT images in the fused images on the right.

making an SURE image for every 3 s of data and then changing the starting time of the processed data across all acquired data. A video of this is also found in the Supplementary Material (rat_59_duration_3sec_interval_0.25sec.mp4 )

G. SURE and ULM Comparison

A comparison between ULM and SURE density images is given in Fig. 17. The rat was scanned with the Verasonics

scanner and the same transducer and position. An amplitude modulation scheme was employed for enhancing the bubble signal with 12 VSs and three emissions for each in an amplitude modulation scheme [51]. The ULM scan time was 46.8 s. Motion compensation, detection, and tracking with a hierarchical Kalman Tracker were employed to create the ULM images [45]. The SURE and ULM images are fused in Fig. 18, where the background in red is the SURE image and the ULM is blended in blue on top. It can be seen

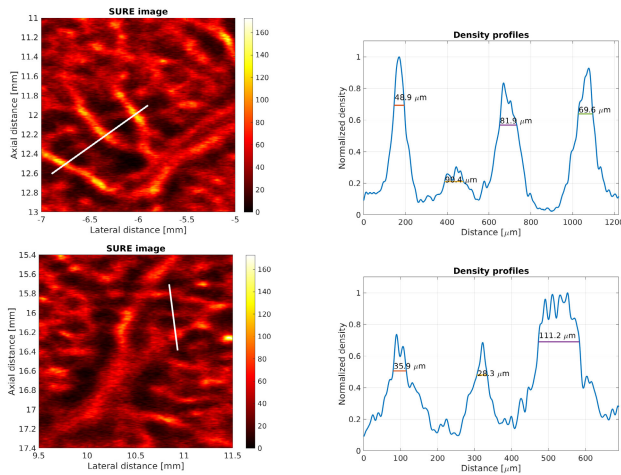


Fig. 12. Quantification of vessel sizes in the SURE image shown in Fig. 9. The white line in the left images shows the position for quantification and the right image is the signal along the line. The relative density of detections is shown as a function of spatial position. The size indicated shows the -3 -dB width of the various vessels.

that the vessels with a size between 50 and $200 \mu\text{m}$ are in close correspondence between the two images and that their position, path, and size are in agreement. The feeding arcuate vessels in the lower part of the images below a depth of 11 mm follow the same path in both images with roughly the same size, although it is difficult to accurately determine their size due to the lack of tracks in the ULM.

VIII. DISCUSSION

The results indicate that SR imaging using erythrocytes as targets is possible. SURE imaging can reveal the microvascular structures of the rat kidney down to vessel sizes of $28 \mu\text{m}$ within seconds. The imaging relies purely on the scattering from erythrocytes, and no patient preparation or contrast agent injection is needed, making this technique fully noninvasive. Therefore, SURE imaging can be used on any patient, where conventional ultrasound is applicable. The method can be used with the full FDA range for MI, probe temperature, and intensity available for normal, clinical ultrasound. The imaging is fast and the data are acquired within seconds. This significantly reduces motion artifacts and makes SURE applicable for microvascular imaging in patients despite body movements and pulsations from respiration and heart beating.

It might be counter intuitive that vessels with sizes below the wavelength can be detected using SURE. Here, it should be kept in mind that the erythrocytes emit a spherical wave when insonified [25] and yield a signal, which will be depicted as the PSF of the system. This is symmetric around the center point of the erythrocyte for proper SA imaging, and detecting the center location, thus, gives a position, which on average lies inside the vessel. Detecting many positions within the vessel will depict the spatial extent of the vessel. The echo canceling processing, using either a filter or SVD processing, removes stationary scatterers, and therefore, only the moving erythrocytes are left. There will be many erythrocytes within a resolution cell, but the complex summation of all scatterers within the vessel will still on average have a peak position

within the vessel. The density functions of the detections shown in the bottom graphs in Figs. 6 and 8 quantify how the detections are distributed within the vessels, where the green dashed lines show the theoretical distribution of the detections given by (2), and the black solid line is the estimated distribution closely matching the theoretical distribution. The area outside the theoretical green curve prediction is proportional to the probability that the hypothesis does not hold.

Fig. 7 shows the SURE density image compared to the theoretical distribution given by (2). For isolated vessels at the top graph, the estimated densities above 0.6 closely follow the theoretical distribution, and their FWHM is around 34% wider at 0.2λ compared to the vessel width of 0.151λ . For the closer lying vessels at the bottom graph, the resulting distributions in red get wider but roughly follow the shape of the theoretical distribution. Having very closely lying vessel produces a two-peak distribution (blue), but this can be avoided by using the estimated velocity direction in the discrimination as in [24].

SURE imaging relies on removing the tissue signal using precise echo canceling. This entails that tissue motion can be compensated for with a precision of micrometers and that out-of-plane motion is negligible. This is in most cases successful, but for large motions or out-of-plane motion, significant tissue components can evolve and can be detected. This will give a large number of detections in roughly the same position and will appear as bright targets in the image. This can be seen as an artifact in the image and is seen in, e.g., Fig. 19 on the top rightmost part of the kidney, where the echo canceling did not fully remove the tissue signal. This can potentially influence the FRC, and this should be calculated from regions without such bright artifacts. Further development of the approach should, thus, include out-of-plane motion, and this can be made if data are acquired in 3-D as in [52], [53], and [54].

The resolution of SURE imaging is determined by how close two objects can be and still get reliably detected and resolved. The Field II simulations shown in Fig. 6 show that vessels with a radius of $12.5 \mu\text{m}$ can be detected and that vessels separated by $70 \mu\text{m}$ can be resolved for a wavelength in tissue of $166 \mu\text{m}$. Subwavelength resolution is, thus, possible after 3 s of data acquisition. Naji et al. [24] using recursive SA imaging and tracking demonstrate that even the last adjacent pair of vessels can be separated due to the opposing flow directions.

SURE and micro-CT images are compared in Fig. 10, where the course of the vessels is consistent between the two image types. It can be noted that the vessels in the micro-CT image with a $20\text{-}\mu\text{m}$ size generally are larger than for the SURE images. This can be due to the MIP employed in the micro-CT slice processing. The MIP has been taken over the out-of-plane thickness of the ultrasound image to mimic the slice thickness of the ultrasound image.

The maximum detection in the SURE image will also only show the strongest flow signal. Larger vessels will have a larger velocity and more signal will pass through the SVD echo canceling. This signal dominates the signal from adjacent smaller vessels, which can be the reason for both the smaller vessel size and the darker area around the major vessels. This effect will be intricately dependent on the echo canceling

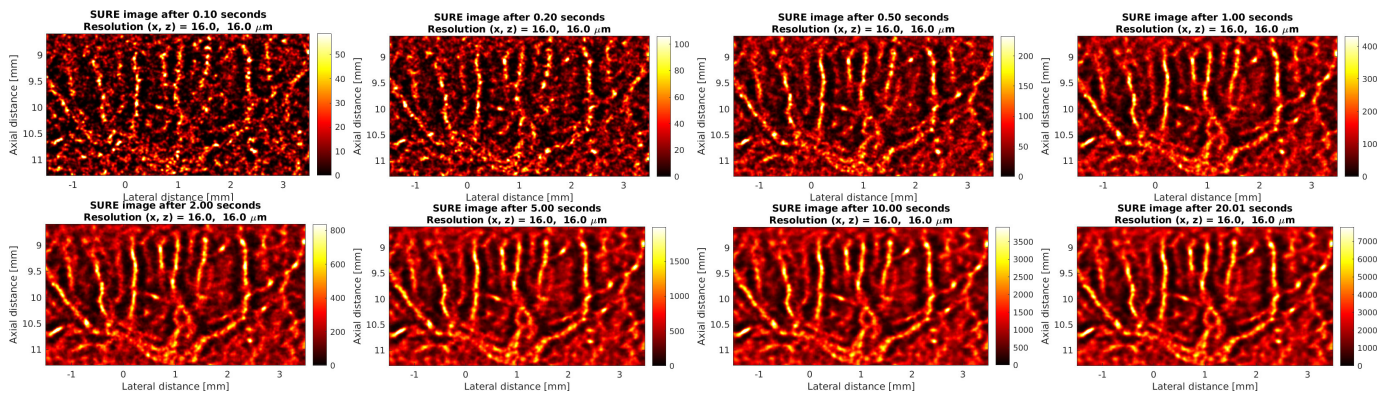


Fig. 13. Evolution of the SURE image over time. The image obtained after 0.1, 0.2, 0.5, 1, 2, 5, 10, and 20 s with the same processing is shown from left to right. The time evolution can also be studied in the accompanying video file: [sure_rat_59_real_time_2023.09.01.mp4](#)

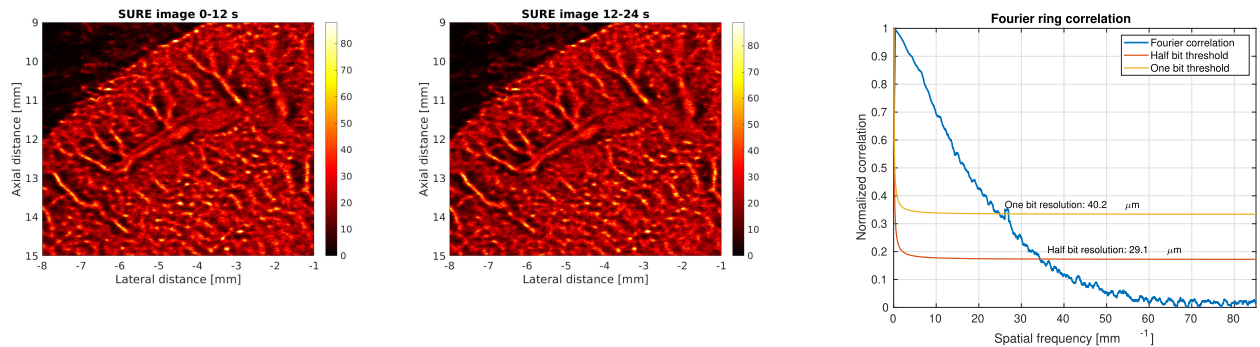


Fig. 14. Two images are used for the FRC calculation. The left zoomed image is for the first 12 s of data and the middle one is for the remaining 12 s. The right graph shows the FRC curve and the thresholds for 1- and 0.5-bit resolutions.

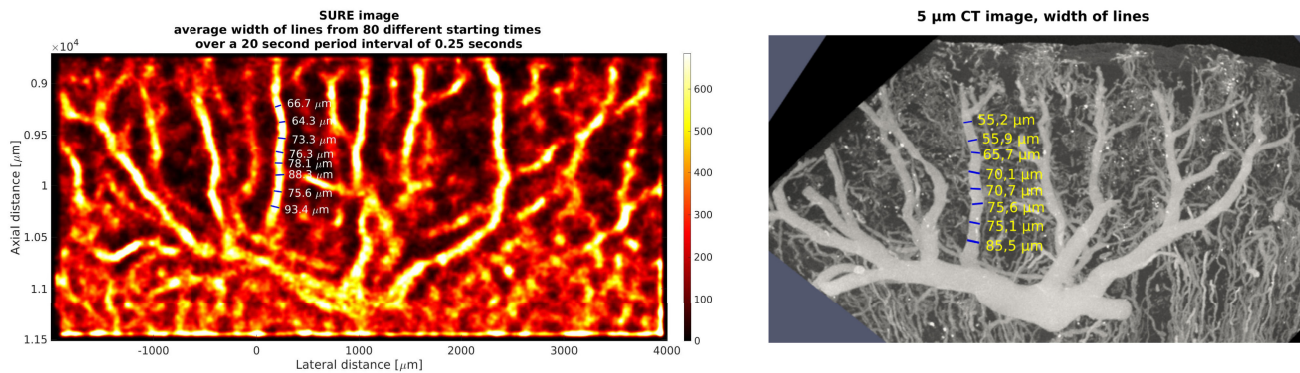


Fig. 15. Comparison of the vessel size between the SURE image (left) and micro-CT scan (right, voxel size $5 \mu\text{m}$). The variation in vessel size for different scan times can also be seen in the Supplementary Video ([rat_59_duration_3sec_interval_0.25sec.mp4](#)).

performed, its parameters used, accuracy of motion estimation and compensation, and the detection threshold. It should also be noted that the SURE image is acquired on live animals, whereas the micro-CT image is acquired over 11 h for a contrast filled excised organ, where the pressure relations have changed compared to a live animal. Therefore, the vessel geometry in the micro-CT is likely to be distorted to some degree.

A $5\text{-}\mu\text{m}$ voxel size micro-CT scan was therefore made to investigate this. A part of the kidney was scanned, as the scan time is very long (20 h) for this subset. The result is shown in Fig. 15, where the vessel size was determined by counting the number of bright pixels. Repeating the experiment with

different datasets with 3 s of data for each SURE image revealed the SD of the vessel size, as shown in Fig. 16. The SURE vessel size was here slightly larger than for the micro-CT scan but was within one to two SDs, and importantly, both imaging modalities showed the increase in vessel size from the distal to the proximal end. The vessel size was between 64.3 and $93.4 \mu\text{m}$ for SURE and between 55.2 and $85.5 \mu\text{m}$ for the micro-CT scan giving a vessel size roughly 2.5 lower than the wavelength and 3.9 times lower than the lateral resolution of the imaging system as indicated by the PSF in Fig. 4. Smaller vessels could also be seen in the SURE image and also seem consistent in the video for the different starting scan times.

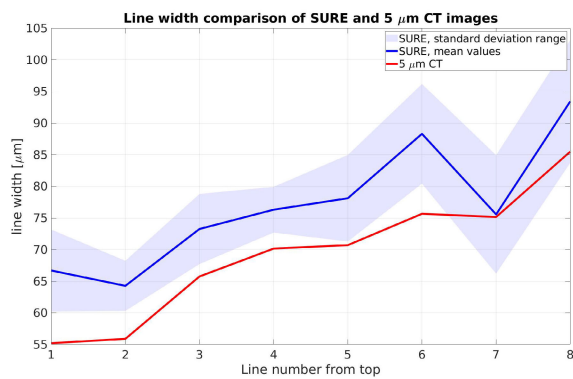


Fig. 16. Quantitative comparison of the vessel size between the SURE image (blue) and micro-CT scan (red, a voxel size of $5 \mu\text{m}$). The shaded blue area indicates one SD for the measure.

Another resolution metric is based on FRC [47], [48], [50], where two similar images are correlated. Splitting the in vivo data into two for generating two 12-s acquisitions gave a 0.5-bit resolution of $29.1 \mu\text{m}$ and a 1-bit resolution of $40.2 \mu\text{m}$. In addition, a vessel with a size of $28.3 \mu\text{m}$ was detected and the precision of detecting vessel size was on average $12.0 \mu\text{m}$. All these measures point to an estimated SURE image resolution of roughly a third to a quarter wavelength (from 50 to $35 \mu\text{m}$) even for acquisition times of 6 s. SR images using SonoVue and a commercial scanner also on Sprague-Dawley rat kidneys gave a mean 1-bit FRC value of approximately $55 \mu\text{m}$ averaged across ten rats [2]. A similar 10-MHz linear array probe was used for the amplitude-modulated linear array scan. The SURE images acquired over 6 s, thus giving a similar resolution as SR images acquired over 10 min. Other ULM pipelines have given resolutions down to $5 \mu\text{m}$ [1] and thus yield higher resolution than SURE. ULM is also better at separating out closely lying vessel due to the isolate bubble response without interference, so the two techniques supplement each other for different applications.

It might well be possible to detect even smaller vessels; the background haze seen in the SURE images may originate from the arterioles, venules, and capillaries surrounding the larger vessels. Maybe an extended acquisition for minutes could reveal clear images of capillaries or an improved processing of the data could give consistent images of smaller vessels. The ultimate limit is currently set by the motion correction, which has errors in the $60 \text{ nm} - 2 \mu\text{m}$ range with the current processing as indicated in Section VII-B. The out-of-plane y -motion is probably also important to compensate for increasing resolution. This can potentially be estimated by using 3-D scanning with, e.g., row-column arrays [52], [54].

A comparison of ULM and SURE images is shown in Fig. 17 and a fused image is shown in Fig. 18. The ULM has a sharper appearance and the ability to separate closer lying vessels than the SURE image for vessel sizes smaller than $50 \mu\text{m}$. A longer SURE acquisition of 46 s shown in Fig. 19 gives a smoother appearing image but does not reveal more or smaller vessels. Smaller vessels are indicated as blurred regions of flow in SURE. The fusion of two closer lying vessels is shown for the two rightmost branches in Fig. 19,

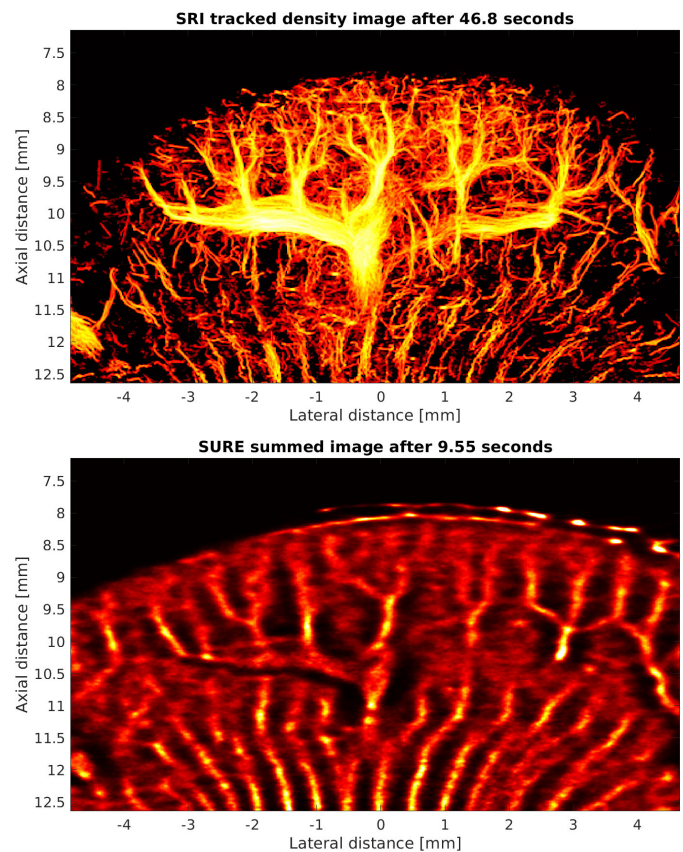


Fig. 17. Comparison of ULM/SRI (top) and SURE (bottom) images acquired on the same Sprague-Dawley rat with the same probe position in the cortex region of the kidney.

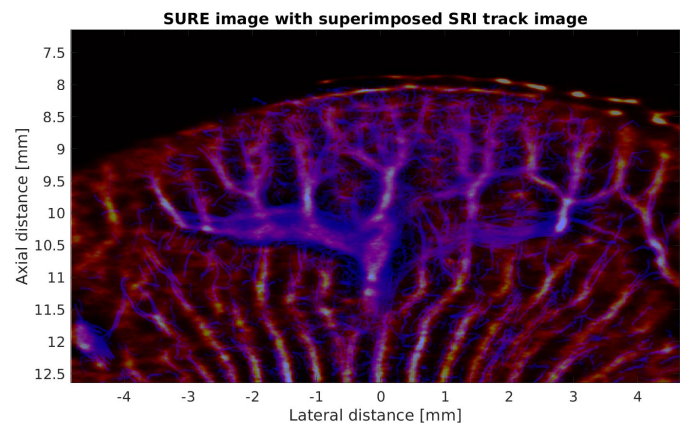


Fig. 18. Fused SURE density image (red) with the SR track image (blue) from Fig. 17 on the top part of the cortex.

region 1, where the ULM displays the rightmost vessel branch, but tracks are also seen around this. The SURE image displays the flow, but not two clearly visible vessels, which is also seen in region 3. In region 2, the SURE image displays two separate vessels, which probably is an artery-vein pair, with the artery in region 2. The ULM displays one large vessel bunch for the density image, and the two vessels can probably only be separated out by mapping the velocity of the flow. The arcuate vessels feeding the kidney cortex are visualized at depths below 11 mm. The flow in the SURE vessels and the ULM track follow the same path, but it is more difficult to follow individual vessels in

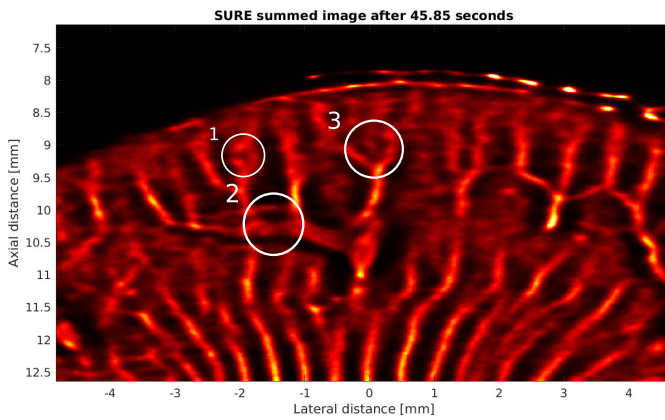


Fig. 19. SURE image acquired over 46 s for the same rat as in Fig. 17. The circles mark regions where ULM and SURE images show the vessels differently.

the ULM due to the sparseness of tracks than in the SURE image. This could be alleviated by having a longer ULM acquisition of minutes. The ULM images appear sharper and can separate closer lying vessels in the image. There are, thus, major differences between the SURE and ULM images. SURE seems to concentrate vessels into bundles with darker regions adjacent to them. This is probably due to a stronger signal from larger vessels, which will dominate the peak detection, making it difficult to visualize small vessels with few scatterers and therefore less signal energy. More individual vessels are seen in ULM, however, with a much sparser distribution due to the few tracks. ULM would, thus, need a longer acquisition time to clearly separate the closely lying vessels. The flow direction seems to be along the same path in both SURE and ULM.

The data processing entails beamforming, motion estimation, SVD, peak detection, and image display. Only the SVD has currently not been implemented for real-time processing on prototype scanners, and this is presently the limiting factor for real-time imaging. This could be solved by employing a fast GPU card and dedicated implementations for potential real-time imaging. An alternative is to use a more conventional and less demanding approach for separating the tissue from the moving erythrocytes as used in normal flow imaging. A version of the SURE pipeline with a simple subtraction echo canceler attained real-time processing on a standard GPU [32]. It is, thus, possible to have real-time microvascular imaging.

In this article, the images were acquired using linear array probes yielding 2-D images. This should be extended to 3-D using matrix probes and 3-D SA imaging. It has recently been shown that row-column arrays can be used for 3-D SR imaging with the contrast agent SonoVue and a $62 + 62$ element array [54]. These arrays have $N + N$ channel connections rather than N^2 for fully populated matrix arrays, where N is the side length of the matrix. Accordingly, 3-D imaging is possible with recording of only N channels, which is the same number of receiving channels used in this article, making SURE imaging translatable to 3-D, when appropriate arrays have been fabricated.

The sequence employed here uses interleaved, spherical transmissions. It is possible to devise a similar sequence using plane waves, which, however, often struggle with probe heating issues not present for SA imaging. The SURE image

quality is dependent on the signal-to-noise ratio, so this might become an issue when the transmit voltage has to be reduced for plane wave imaging.

Modalities for noninvasive microvascular imaging are necessary, as microvascular disruption plays a part in diseases throughout the body, including in the kidneys [55]. The diseases include diabetes, hypertension, cancer, and ischemic disease, which are all clinically very relevant due to their increasing prevalence. In diabetes, renal microvascular alterations [56] ultimately decrease renal function. For tumors, the microvasculature is morphologically and functionally anomalous [57]. Common to microvascular diseases is that early diagnosis and monitoring of progression and treatment response have substantial clinical potential. For example, for persons with diabetes, it is not fully understood who develops diabetic nephropathy and who does not. If microvascular imaging could reveal pathological vessel changes before the irreversible renal tissue damage occurs, early reno-protective treatment could potentially improve the course of the disease. Treatment monitoring for persons with solid tumors relies on tumor size evaluation according to the RECIST criteria [58]. Often, weeks or months pass from treatment initiation until the tumor response is evaluated. However, pre-clinical studies have shown that intratumoral microvascular alterations can occur before a change in tumor size can be detected [59], [60]. Therefore, microvascular imaging could help determine whether a person is a nonresponder to a specific treatment regimen and allow earlier change of treatment strategy.

IX. CONCLUSION

SURE imaging can detect vessels in the microcirculation down to sizes of $28 \mu\text{m}$: six times smaller than the employed wavelength. Simulations and FRC indicate a resolution between 29 and $70 \mu\text{m}$ for a wavelength of $166 \mu\text{m}$. A further increase in resolution can be attained by also using tracking as is described in [24]. The imaging can be conducted without injection of contrast agents, and there are, thus, no other restrictions on MI than those set by the current standards for clinical ultrasound imaging. The images are acquired in 1–10 s, which minimizes motion artifacts and makes them applicable for normal, clinical use, and real-time implementation is possible. The technique offers great future possibilities for improving our understanding of normal microvascular physiology as well as microvascular alterations in disease development and progression, ultimately improving the prognosis for a great variety of persons with microvascular diseases.

ACKNOWLEDGMENT

Jørgen Arendt Jensen, Mostafa Amin Najj, Sebastian Kazmarek Præsius, Iman Taghavi, Lauge Naur Hansen, and Borislav Gueorguiev Tomov are with the Center for Fast Ultrasound Imaging, Department of Health Technology, Technical University of Denmark, 2800 Kongens Lyngby, Denmark (e-mail: jaje@dtu.dk; mamna@dtu.dk; sebka@dtu.dk; lnaha@dtu.dk; bgto@dtu.dk).

Mikkel Schou is with BK Medical, GE Healthcare, 2730 Herlev, Denmark (e-mail: mmikkelschou@gmail.com).

Sofie Bech Andersen, Stinne Byrholdt Søgaard, Nathalie Sarup Panduro, and Michael Bachmann Nielsen are with the Department of Biomedical Sciences, University of Copenhagen, 1172 Copenhagen, Denmark, and also with the Department of Radiology, Rigshospitalet,

2100 Copenhagen, Denmark (e-mail: posttilsofiebeck@gmail.com; stinnebyrholdt@gmail.com; nathalie.sarup.panduro.01@regionh.dk; mbn@dadlnet.dk).

Charlotte Mehlin Sørensen is with the Department of Biomedical Sciences, University of Copenhagen, 1172 Copenhagen, Denmark (e-mail: cmehlin@sund.ku.dk).

Carsten Gundlach is with the Department of Physics, Technical University of Denmark, 2800 Kongens Lyngby, Denmark (e-mail: cagu@fysik.dtu.dk).

Hans Martin Kjer and Anders Bjorholm Dahl are with DTU Compute, Technical University of Denmark, 2800 Kongens Lyngby, Denmark (e-mail: hmkj@dtu.dk; abda@dtu.dk).

Martin Lind Ommen and Erik Vilain Thomsen are with the MEMS Group, Department of Health Technology, Technical University of Denmark, 2800 Kongens Lyngby, Denmark (e-mail: marlio@dtu.dk; ervt@dtu.dk).

Niels Bent Larsen is with the Engineered Fluidics and Tissues Group, Department of Health Technology, Technical University of Denmark, 2800 Kongens Lyngby, Denmark (e-mail: nibl@dtu.dk).

REFERENCES

- [1] K. Christensen-Jeffries et al., “Super-resolution ultrasound imaging,” *Ultrasound Med. Biol.*, vol. 46, no. 4, pp. 865–891, 2020.
- [2] I. Taghavi, S. B. Andersen, C. A. V. Hoyos, M. B. Nielsen, C. M. Sørensen, and J. A. Jensen, “In vivo motion correction in super-resolution imaging of rat kidneys,” *IEEE Trans. Ultrason., Ferroelectr., Freq. Control*, vol. 68, no. 10, pp. 3082–3093, Oct. 2021.
- [3] C. Errico et al., “Ultrafast ultrasound localization microscopy for deep super-resolution vascular imaging,” *Nature*, vol. 527, no. 7579, pp. 499–502, Nov. 2015.
- [4] O. M. Viessmann, R. J. Eckersley, K. Christensen-Jeffries, M. X. Tang, and C. Dunsby, “Acoustic super-resolution with ultrasound and microbubbles,” *Phys. Med. Biol.*, vol. 58, no. 18, pp. 6447–6458, Sep. 2013.
- [5] M. A. O’Reilly and K. Hynynen, “A super-resolution ultrasound method for brain vascular mapping,” *Med. Phys.*, vol. 40, no. 11, pp. 110701–110707, Nov. 2013.
- [6] Y. Desailly, J. Pierre, O. Couture, and M. Tanter, “Resolution limits of ultrafast ultrasound localization microscopy,” *Phys. Med. Biol.*, vol. 60, no. 22, pp. 8723–8740, Nov. 2015.
- [7] K. Christensen-Jeffries, R. J. Browning, M. X. Tang, C. Dunsby, and R. J. Eckersley, “In vivo acoustic super-resolution and super-resolved velocity mapping using microbubbles,” *IEEE Trans. Med. Imag.*, vol. 34, no. 2, pp. 433–440, Feb. 2015.
- [8] D. Ackermann and G. Schmitz, “Detection and tracking of multiple microbubbles in ultrasound B-mode images,” *IEEE Trans. Ultrason., Ferroelectr., Freq. Control*, vol. 63, no. 1, pp. 72–82, Jan. 2016.
- [9] S. B. Andersen et al., “Super-resolution imaging with ultrasound for visualization of the renal microvasculature in rats before and after renal ischemia: A pilot study,” *Diagnostics*, vol. 10, no. 11, p. 862, Oct. 2020.
- [10] T. Opacic et al., “Motion model ultrasound localization microscopy for preclinical and clinical multiparametric tumor characterization,” *Nature Commun.*, vol. 9, no. 1, p. 1527, 2018.
- [11] C. Demeñé et al., “Transcranial ultrafast ultrasound localization microscopy of brain vasculature in patients,” *Nature Biomed. Eng.*, vol. 5, no. 3, pp. 219–228, Mar. 2021.
- [12] V. Hingot, C. Errico, B. Heiles, L. Rahal, M. Tanter, and O. Couture, “Microvascular flow dictates the compromise between spatial resolution and acquisition time in ultrasound localization microscopy,” *Sci. Rep.*, vol. 9, no. 1, pp. 1–10, Feb. 2019.
- [13] K. B. Hansen et al., “Robust microbubble tracking for super resolution imaging in ultrasound,” in *Proc. IEEE Int. Ultrason. Symp. (IUS)*, Sep. 2016, pp. 1–4.
- [14] J. Foiret, H. Zhang, T. Ilvovtsh, L. Mahakian, S. Tam, and K. W. Ferrara, “Ultrasound localization microscopy to image and assess microvasculature in a rat kidney,” *Sci. Rep.*, vol. 7, no. 1, p. 13662, Oct. 2017.
- [15] V. Hingot, C. Errico, M. Tanter, and O. Couture, “Subwavelength motion-correction for ultrafast ultrasound localization microscopy,” *Ultrasonics*, vol. 77, pp. 17–21, May 2017.
- [16] S. Harput et al., “Two-stage motion correction for super-resolution ultrasound imaging in human lower limb,” *IEEE Trans. Ultrason., Ferroelectr., Freq. Control*, vol. 65, no. 5, pp. 803–814, May 2018.
- [17] M. Piepenbrock, S. Dencks, and G. Schmitz, “Reliable motion estimation in super-resolution U.S. by reducing the interference of microbubble movement,” in *Proc. IEEE Int. Ultrason. Symp. (IUS)*, Oct. 2019, pp. 384–387.
- [18] T. M. Kierski et al., “Superharmonic ultrasound for motion-independent localization microscopy: Applications to microvascular imaging from low to high flow rates,” *IEEE Trans. Ultrason., Ferroelectr., Freq. Control*, vol. 67, no. 5, pp. 957–967, May 2020.
- [19] J. H. Park, W. Choi, G. Y. Yoon, and S. J. Lee, “Deep learning-based super-resolution ultrasound speckle tracking velocimetry,” *Ultrasound Med. Biol.*, vol. 46, no. 3, pp. 598–609, Mar. 2020.
- [20] A. Bar-Zion, O. Solomon, C. Rabut, D. Maresca, Y. C. Eldar, and M. G. Shapiro, “Doppler slicing for ultrasound super-resolution without contrast agents,” *BioRxiv*, pp. 1–10, Nov. 2021, doi: 10.1101/2021.11.19.469083.
- [21] Q. You et al., “Contrast-free super-resolution power Doppler (CS-PD) based on deep neural networks,” *IEEE Trans. Ultrason., Ferroelectr., Freq. Control*, vol. 70, no. 10, pp. 1355–1368, Oct. 2023.
- [22] J. A. Jensen et al., “Fast super resolution ultrasound imaging using the erythrocytes,” *Proc. SPIE*, vol. 12038, Apr. 2022, Art. no. 120380.
- [23] J. A. Jensen et al., “In vivo super resolution ultrasound imaging using the erythrocytes—SURE,” in *Proc. IEEE Int. Ultrason. Symp. (IUS)*, Oct. 2022, pp. 1–4.
- [24] M. A. Naji et al., “Super resolution ultrasound imaging using the erythrocytes: Part II: Velocity images,” *IEEE Trans. Ultrason., Ferroelectr., Freq. Control*, vol. 71, no. 8, pp. 945–959, Aug. 2024.
- [25] J. A. Jensen, “A model for the propagation and scattering of ultrasound in tissue,” *J. Acoust. Soc. Amer.*, vol. 89, no. 1, pp. 182–190, Jan. 1991.
- [26] J. A. Jensen, S. Nikolov, K. L. Gammelmark, and M. H. Pedersen, “Synthetic aperture ultrasound imaging,” *Ultrasonics*, vol. 44, pp. e5–e15, Dec. 2006.
- [27] J. A. Jensen, B. G. Tomov, L. E. Haslund, N. S. Panduro, and C. M. Sørensen, “Universal synthetic aperture sequence for anatomic, functional, and super resolution imaging,” *IEEE Trans. Ultrason., Ferroelectr., Freq. Control*, vol. 70, no. 7, pp. 708–720, Jul. 2023.
- [28] M. B. Stuart et al., “Real-time volumetric synthetic aperture software beamforming of row–column probe data,” *IEEE Trans. Ultrason., Ferroelectr., Freq. Control*, vol. 68, no. 8, pp. 2608–2618, Aug. 2021.
- [29] G. E. Trahey, J. W. Allison, and O. T. von Ramm, “Angle independent ultrasonic detection of blood flow,” *IEEE Trans. Biomed. Eng.*, vol. BME-34, no. 12, pp. 965–967, Dec. 1987.
- [30] J. A. Jensen and P. Munk, “A new method for estimation of velocity vectors,” *IEEE Trans. Ultrason., Ferroelectr., Freq. Control*, vol. 45, no. 3, pp. 837–851, May 1998.
- [31] J. A. Jensen, “A new estimator for vector velocity estimation,” *IEEE Trans. Ultrason., Ferroelectr., Freq. Control*, vol. 48, no. 4, pp. 886–894, Jul. 2001.
- [32] S. K. Præsius, M. B. Stuart, M. Schou, B. Dammann, H. H. B. Sørensen, and J. A. Jensen, “Real-time super-resolution ultrasound imaging using GPU acceleration,” in *Proc. IEEE Int. Ultrason. Symp. (IUS)*, Oct. 2022, pp. 1–4.
- [33] C. Demeñé et al., “Spatiotemporal clutter filtering of ultrafast ultrasound data highly increases Doppler and fUltrasound sensitivity,” *IEEE Trans. Med. Imag.*, vol. 34, no. 11, pp. 2271–2285, Nov. 2015.
- [34] P. Song, A. Manduca, J. D. Trzasko, and S. Chen, “Ultrasound small vessel imaging with block-wise adaptive local clutter filtering,” *IEEE Trans. Med. Imag.*, vol. 36, no. 1, pp. 251–262, Jan. 2017.
- [35] J. Baranger, B. Arnal, F. Perren, O. Baud, M. Tanter, and C. Demeñé, “Adaptive spatiotemporal SVD clutter filtering for ultrafast Doppler imaging using similarity of spatial singular vectors,” *IEEE Trans. Med. Imag.*, vol. 37, no. 7, pp. 1574–1586, Jul. 2018.
- [36] P. A. Yushkevich et al., “User-guided 3D active contour segmentation of anatomical structures: Significantly improved efficiency and reliability,” *NeuroImage*, vol. 31, no. 3, pp. 1116–1128, Jul. 2006.
- [37] J. A. Jensen and N. B. Svendsen, “Calculation of pressure fields from arbitrarily shaped, apodized, and excited ultrasound transducers,” *IEEE Trans. Ultrason., Ferroelectr., Freq. Control*, vol. 39, no. 2, pp. 262–267, Mar. 1992.
- [38] J. A. Jensen, “FIELD: A program for simulating ultrasound systems,” in *Proc. 10th Nordic-Baltic Biomed. Imag.*, Mar. 1996, vol. 34, no. 1, pp. 351–353.
- [39] J. A. Jensen, “A multi-threaded version of field II,” in *Proc. IEEE Int. Ultrason. Symp.*, Sep. 2014, pp. 2229–2232.
- [40] J.-B. Michel and J. L. Martin-Ventura, “Red blood cells and hemoglobin in human atherosclerosis and related arterial diseases,” *Int. J. Mol. Sci.*, vol. 21, no. 18, p. 6756, Sep. 2020.
- [41] M. L. Ommen, M. Schou, C. Beers, J. A. Jensen, N. B. Larsen, and E. V. Thomsen, “3D printed calibration micro-phantoms for super-resolution ultrasound imaging validation,” *Ultrasonics*, vol. 114, Jul. 2021, Art. no. 106353.

- [42] G. A. Brock-Fischer, M. D. Poland, and P. G. Rafter, "Means for increasing sensitivity in non linear ultrasound systems," U.S. Patent 5 577 505, Nov. 26, 1996.
- [43] D. Fouan and A. Bouakaz, "Investigation of classical pulse sequences for contrast-enhanced ultrasound imaging with a cMUT probe," *IEEE Trans. Ultrason., Ferroelectr., Freq. Control*, vol. 63, no. 10, pp. 1496–1504, Oct. 2016.
- [44] B. G. Tomov, R. Daigle, and J. Jensen, "Ten-minute continuous acquisitions with the verasonics vantage research scanner," in *Proc. IEEE Ultrason. Symp.*, Sep. 2023, pp. 1–3.
- [45] I. Taghavi et al., "Ultrasound super-resolution imaging with a hierarchical Kalman tracker," *Ultrasonics*, vol. 122, May 2022, Art. no. 106695.
- [46] C. Kasai, K. Namekawa, A. Koyano, and R. Omoto, "Real-time two-dimensional blood flow imaging using an autocorrelation technique," *IEEE Trans. Son. Ultrason.*, vol. SU-32, no. 3, pp. 458–463, May 1985.
- [47] R. P. J. Nieuwenhuizen et al., "Measuring image resolution in optical nanoscopy," *Nature Methods*, vol. 10, no. 6, pp. 557–562, Jun. 2013.
- [48] N. Banterle, K. H. Bui, E. A. Lemke, and M. Beck, "Fourier ring correlation as a resolution criterion for super-resolution microscopy," *J. Structural Biol.*, vol. 183, no. 3, pp. 363–367, Sep. 2013.
- [49] V. Hingot, A. Chavignon, B. Heiles, and O. Couture, "Measuring image resolution in ultrasound localization microscopy," *IEEE Trans. Med. Imag.*, vol. 40, no. 12, pp. 3812–3819, Dec. 2021.
- [50] M. van Heel and M. Schatz, "Fourier shell correlation threshold criteria," *J. Struct. Biol.*, vol. 151, no. 3, pp. 250–262, Sep. 2005.
- [51] R. J. Eckersley, C. T. Chin, and P. N. Burns, "Optimising phase and amplitude modulation schemes for imaging microbubble contrast agents at low acoustic power," *Ultrasound Med. Biol.*, vol. 31, no. 2, pp. 213–219, Feb. 2005.
- [52] B. Heiles et al., "Ultrafast 3D ultrasound localization microscopy using a 32×32 matrix array," *IEEE Trans. Ultrason., Ferroelectr., Freq. Control*, vol. 38, no. 9, pp. 2005–2015, Sep. 2019.
- [53] F. Lin, S. E. Shelton, D. Espíndola, J. D. Rojas, G. Pinton, and P. A. Dayton, "3-D ultrasound localization microscopy for identifying microvascular morphology features of tumor angiogenesis at a resolution beyond the diffraction limit of conventional ultrasound," *Theranostics*, vol. 7, no. 1, pp. 196–204, 2017.
- [54] J. A. Jensen et al., "Three-dimensional super-resolution imaging using a row-column array," *IEEE Trans. Ultrason., Ferroelectr., Freq. Control*, vol. 67, no. 3, pp. 538–546, Mar. 2020.
- [55] B. A. Corliss, C. Mathews, R. Doty, G. Rohde, and S. M. Peirce, "Methods to label, image, and analyze the complex structural architectures of microvascular networks," *Microcirculation*, vol. 26, no. 5, Jul. 2019, Art. no. e12520.
- [56] K. Drummond and M. Mauer, "The early natural history of nephropathy in type 1 diabetes: II. Early renal structural changes in type 1 diabetes," *Diabetes*, vol. 51, no. 5, pp. 1580–1587, 2002.
- [57] J. Ehling et al., "Micro-CT imaging of tumor angiogenesis: Quantitative measures describing micromorphology and vascularization," *Amer. J. Pathol.*, vol. 184, no. 2, pp. 431–441, 2014.
- [58] L. H. Schwartz et al., "RECIST 1.1—Update and clarification: From the RECIST committee," *Eur. J. Cancer*, vol. 62, pp. 132–137, Jul. 2016.
- [59] J. D. Rojas et al., "Ultrasound measurement of vascular density to evaluate response to anti-angiogenic therapy in renal cell carcinoma," *IEEE Trans. Biomed. Eng.*, vol. 66, no. 3, pp. 873–880, Mar. 2019.
- [60] S. K. Kasoji, J. N. Rivera, R. C. Gessner, S. X. Chang, and P. A. Dayton, "Early assessment of tumor response to radiation therapy using high-resolution quantitative microvascular ultrasound imaging," *Theranostics*, vol. 8, no. 1, pp. 156–168, 2018.



Jørgen Arendt Jensen (Fellow, IEEE) received the Master of Science degree in electrical engineering and the Ph.D. and Dr.Techn. degrees from the Technical University of Denmark, Kongens Lyngby, Denmark, in 1985, 1989, and 1996, respectively.

Since 1993, he has been a Full Professor of biomedical signal processing with the Department of Health Technology, Technical University of Denmark. He has been the Head of the Center for Fast Ultrasound Imaging (CFU), Technical University of Denmark, since 1998. He has been a Visiting Scientist at

Duke University, Durham, NC, USA; Stanford University, Stanford, CA, USA; and the University of Illinois at Urbana–Champaign, Urbana–Champaign, IL, USA. He has been the Head of the Ultrasound and Biomechanics Section since 2020. In 2003, he was one of the founders of the Biomedical Engineering Program in medicine and technology, which is a joint degree program between the Technical University of Denmark and the Faculty of Health and Medical Sciences, University of Copenhagen, Copenhagen, Denmark (the degree is one of the most sought-after engineering degrees in Denmark). He was the Head of the Study Board from 2003 to 2010 and an Adjunct Professor with the University of Copenhagen from 2005 to 2010. Fifty-five Ph.D. students have graduated from CFU. He has published more than 550 journal articles and conference papers on signal processing and medical ultrasound and the book *Estimation of Blood Velocities Using Ultrasound* (Cambridge Univ. Press, 1996). He is also the developer and the maintainer of the Field II simulation program. He has given a number of short courses on simulation, synthetic aperture imaging, and flow estimation at international scientific conferences and teaches biomedical signal processing and medical imaging at the Technical University of Denmark. His research is centered around simulation of ultrasound imaging, synthetic aperture imaging, vector blood flow estimation, construction of ultrasound research systems, fast 3-D super-resolution imaging, and their clinical translation.

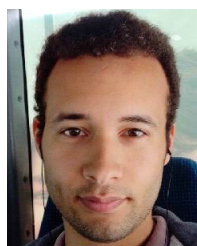
Dr. Jensen has given more than 70 invited talks at international meetings and received several awards for his research, most recently the Grand Solutions Prize from the Danish Minister of Science, the order of Dannebrog by her Majesty the Queen of Denmark, the Rayleigh Award from the IEEE Ultrasonics, Ferroelectrics, and Frequency Control Society (UFFC), and the prestigious Synergy Grant from European Research Council (ERC).



Mostafa Amin Naji (Graduate Student Member, IEEE) received the B.Sc. and M.Sc. degrees in electrical and computer engineering–communication systems from Babol Noshirvani University of Technology (BNUT), Babol, Iran, in 2015 and 2018, respectively. He is currently pursuing the Ph.D. degree in super-resolution ultrasound imaging using the erythrocytes (SURE) with the Center for Fast Ultrasound Imaging (CFU), Technical University of Denmark (DTU), Kongens Lyngby, Denmark.

He has published several papers in journals and conferences on topics related to computer vision, deep learning, image fusion, and super-resolution ultrasound imaging. His research interests include computer vision, deep/machine learning, image/video/signal processing, medical image/signal analysis, and super-resolution ultrasound imaging.

Mr. Amin Naji's B.Sc. thesis, titled "New Multi-Focus Image Fusion Methods in Discrete Cosine Transform," received the Outstanding IEEE B.Sc. Thesis Prize from the IEEE Iran Section Award in 2016. His M.Sc. thesis, titled "Image Fusion Using Deep Learning," was awarded the 2019 Best Thesis Prize by Iranian Society of Machine Vision and Image Processing (ISMVIP).



Sebastian Kazmarek Præsius (Graduate Student Member, IEEE) received the M.Sc. degree in mathematical modeling and computation from the Technical University of Denmark (DTU), Kongens Lyngby, Denmark, in 2022, where he is currently pursuing the Ph.D. degree with the Center for Fast Ultrasound Imaging, with a focus on real-time 2-D and 3-D beamforming, motion estimation, and super-resolution.

His research interests include GPU acceleration, deep learning, and computer graphics.



Iman Taghavi (Member, IEEE) received the bachelor's and master's degrees in electrical engineering from the University of Isfahan, Isfahan, Iran, in 2016, and the Ph.D. degree in super-resolution ultrasound imaging from the Technical University of Denmark, Kongens Lyngby, Denmark, in 2022.

He is currently with the Center for Fast Ultrasound Imaging, Department of Health Technology, Technical University of Denmark, as a Postdoctoral Researcher. He has successfully implemented several digital systems and developed compressed sensing radars, achieving a significant reduction to 2% of the Nyquist criteria. His recent work has focused on the development of an advanced signal processing pipeline for tracking microbubbles inside the bloodstream for super-resolution imaging. His research interests include signal processing and its applications in radars, array sensors, and biomedical imaging.



Stinne Byrholdt Søgaard received the Ph.D. degree in preclinical ultrasound super-resolution imaging in collaboration between the Department of Biomedical Sciences, University of Copenhagen, Copenhagen, Denmark; the Department of Radiology, Rigshospitalet, Copenhagen; and the Center for Fast Ultrasound Imaging, Technical University of Denmark, Kongens Lyngby, Denmark, in 2023.



Mikkel Schou (Member, IEEE) received the M.Sc. and Ph.D. degrees in 3-D ultrasound perfusion imaging from the Technical University of Denmark, Kongens Lyngby, Denmark, in 2017 and 2020, respectively. The topic of his research focused on row-column transducer arrays for perfusion and super-resolution imaging.

He is currently with BK Medical, GE Healthcare, Herlev, Denmark, as an Ultrasound Specialist.



Nathalie Sarup Panduro received the master's degree in medicine from the University of Copenhagen, Copenhagen, Denmark, in 2015. She is currently pursuing the Ph.D. degree in clinical and preclinical super-resolution ultrasound imaging with the Department of Diagnostic Radiology, Rigshospitalet, Copenhagen.



Lauge Naur Hansen (Graduate Student Member, IEEE) received the M.Sc. degree in quantitative biology and disease modeling from the Technical University of Denmark (DTU), Kongens Lyngby, Denmark, in 2022, where he is currently pursuing the Ph.D. degree with the Center for Fast Ultrasound Imaging, with a focus on validation of super-resolution ultrasound imaging techniques by quantitative comparisons with high-resolution computed tomography scans.



Charlotte Mehlin Sørensen received the B.Sc. degree in biology, the M.Sc. degree in human biology, and the Ph.D. degree in renal physiology from the University of Copenhagen (UCPH), Copenhagen, Denmark, in 1996, 1999, and 2004, respectively.

After her Ph.D. degree, she continued as an Assistant Professor at UCPH until 2006, where she joined the medical company Zealand Pharma, Søborg, Denmark, as a Drug Discovery Scientist focusing on acute kidney injury. She returned to UCPH in 2007, where she became an Associate Professor of renal physiology in 2011. Her research focuses on renal hemodynamics and the interplay between the renal autoregulatory mechanisms and the topology of the renal vascular tree and includes the regulatory roles of gap junctions, potassium channels, and incretin hormones.



Sofie Bech Andersen received the master's degree in medicine from the University of Copenhagen, Copenhagen, Denmark, in 2015, and the Ph.D. degree in preclinical ultrasound super-resolution imaging in collaboration between the Department of Biomedical Sciences, University of Copenhagen; the Department of Radiology, Rigshospitalet, Copenhagen; the Center for Fast Ultrasound Imaging, Technical University of Denmark, Kongens Lyngby, Denmark; and BK Medical, Herlev, Denmark,

in 2022.

She was concluding a year as a Resident (introductory position) in radiology with Rigshospitalet. Her research interest includes the development of diagnostic imaging tools for use in the clinic.



Michael Bachmann Nielsen received the Medical degree from the Faculty of Health Science, University of Copenhagen, Copenhagen, Denmark, in 1985, and the Ph.D. and Dr.Med. degrees from the University of Copenhagen in 1994 and 1998, respectively.

He is currently a Full Professor of oncoradiology with the University of Copenhagen and a Consultant with the Department of Radiology, Rigshospitalet, Copenhagen. He has authored over 275 peer-reviewed journal articles on ultrasound or radiology. His current research interests include clinical testing of new ultrasound techniques, tumor vascularity, ultrasound elastography, training in ultrasound, and artificial intelligence.



Carsten Gundlach received the Ph.D. degree in physics from the University of Copenhagen, Copenhagen, Denmark, Denmark, in 2006.

He is currently a Senior Researcher with the Department of Physics, Technical University of Denmark, Kongens Lyngby, Denmark.



Hans Martin Kjer received the Ph.D. degree from the Technical University of Denmark, Kongens Lyngby, Denmark, in 2015.

He currently holds a postdoctoral position and works on image processing and analysis from computed tomography and magnetic resonance imaging.



Anders Bjorholm Dahl (Member, IEEE) is currently a Professor in 3-D image analysis and the Head of the Section for Visual Computing, Department of Applied Mathematics and Computer Science, Technical University of Denmark (DTU), Kongens Lyngby, Denmark. He is heading the Center for Quantification of Imaging Data from MAX IV, Technical University of Denmark, focusing on quantitative analysis of 3-D images. His research is focused on image segmentation and its applications.



Borislav Gueorguiev Tomov (Member, IEEE) received the M.Sc. degree in electronics engineering from the Technical University of Sofia, Sofia, Bulgaria, in 1996, and the Ph.D. degree in medical electronics from the Technical University of Denmark, Kongens Lyngby, Denmark, in 2003.

He is currently a Senior Researcher with the Center for Fast Ultrasound Imaging, Department of Health Technology, Technical University of Denmark. His research interests include medical

ultrasound signal processing and ultrasound scanner architectures and implementations.



Martin Lind Ommen (Member, IEEE) received the M.Sc. degree in physics and nanotechnology from the Technical University of Denmark, Kongens Lyngby, Denmark, in 2017, and the Ph.D. degree from the Biomedical Engineering Section, Department of Health Technology, Technical University of Denmark, in 2020.

His current research interests include microfabrication and nanofabrication in general, in particular the fabrication of capacitive micromachined ultrasonic transducers (CMUTs), as well as phantom fabrication, with a current focus on stereolithographic fabrication of microflow and scatter phantoms.



Niels Bent Larsen (Member, IEEE) received the M.Sc. and Ph.D. degrees in chemistry from the University of Copenhagen, Copenhagen, Denmark, in 1993 and 1997, respectively.

He is currently a Professor and the Section Head of the Department of Health Technology, Technical University of Denmark, Kongens Lyngby, Denmark. His current research interests are in high-resolution 3-D printing of compliant hydrogel materials to recreate the vascular network of body organs to enable

advanced in vitro organ models.



Erik Vilain Thomsen (Member, IEEE) was born in Aarhus, Denmark, in 1964. He received the M.Sc. degree in physics from the University of Southern Denmark, Odense, Denmark, in 1992, and the Ph.D. degree in electrical engineering from the Technical University of Denmark (DTU), Kongens Lyngby, Denmark, in 1998.

He is currently a Professor with the Department of Health Technology, DTU, where he is also the Head of the MEMS Applied Sensors Group and the Head of the division with responsibility for education in healthcare engineering. He teaches classes in solid-state electronics, microtechnology, and nanofabrication and microfabrication. His current research interests include all aspects of capacitive micromachined ultrasonic transducers (CMUTs), general MEMS technology, and piezoelectric MEMS.

Dr. Thomsen received the Danish National Advanced Technology Foundation's Grand Solution Prize in 2017, the AEG Electron Prize in 1995, and several teaching awards at DTU.